10/4/14/89 M.L.L. (1)

SANDIA REPORT

SAND89—1461 • UC—704
Unlimited Release
Printed July 1989

Shock Compression and Release in High-Strength Ceramics

Marlin E. Kipp, Dennis E. Grady

Prepared by
Sandia National Laboratories
Albuquerque, New Mexico 87185 and Livermore, California 94550
for the United States Department of Energy
under Contract DE-AC04-76DP00789

Issued by Sandia National Laboratories, operated for the United States Department of Energy by Sandia Corporation.

Printed in the United States of America. This report has been reproduced directly from the best available copy.

Available to DOE and DOE contractors from
Office of Scientific and Technical Information
PO Box 62
Oak Ridge, TN 37831

Prices available from (615) 576-8401, FTS 626-8401

Available to the public from
National Technical Information Service
US Department of Commerce
5285 Port Royal Rd
Springfield, VA 22161

NTIS price codes
Printed copy: A04
Microfiche copy: A01

Distribution
Category UC-704

SAND89-1461
Unlimited Release
Printed August 1989

SAND--89-1461

DE89 013995

SHOCK COMPRESSION AND RELEASE IN HIGH-STRENGTH CERAMICS

by

Marlin E. Kipp and Dennis E. Grady
Sandia National Laboratories
Albuquerque, New Mexico 87185

ABSTRACT

A preliminary investigation of shock compression and release properties has been performed on four ceramics: silicon carbide, titanium diboride, boron carbide and zirconium dioxide. Eight planar impact experiments using thin discs of similar ceramic as impactor and target have been completed. The particle velocity history at the interface between the back of the target ceramic and a lithium fluoride window material was acquired with a laser velocity interferometer (VISAR). These wave profiles indicate that each of these materials responds in a unique way to shock loading. Peak impact stresses in these experiments range between 20 and 50 GPa, leading to pronounced permanent deformation behavior of these materials. Dynamic compression and release stress-strain behavior of the ceramics, formulated with numerical iteration methods, is compared with compressive strength properties determined from the experimental data. The current experiments provide data for these ceramic materials which can be used to evaluate computational material models in wave propagation codes.

Contents

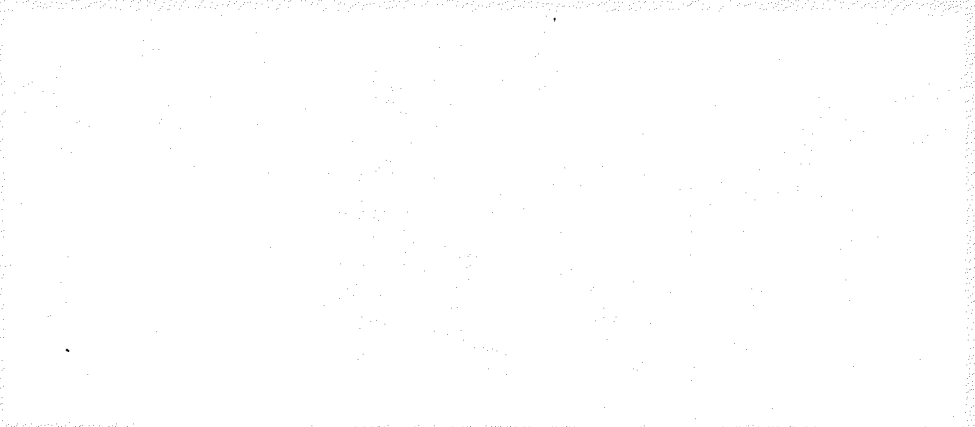

List of Figures

1. Introduction

Ceramics have been repeatedly demonstrated to be effective armor materials against a variety of threats (*e.g.* Wilkins, *et al.*, 1969). However, there are major gaps in the data required for dynamic characterization of these materials. In contrast, quasistatic characterization of ceramics is much more extensive, including data on material structure, metallographic analysis, ultrasonic wave velocities, fracture toughness, *etc.* (Viechnicki, *et al.*, 1987). The most complete collection of Hugoniot data has been assembled by Gust and Royce (1971) and Gust, *et al.* (1973), including Hugoniot elastic limits (HEL) and shock Hugoniots for about a dozen ceramic materials. From other accessible sources, aluminum oxides appear to have received the most attention, with data available for a variety of grades of this material (Ahrens, *et al.*, 1968; Cagnoux and Longy, 1988; Munson and Lawrence, 1979; Rosenberg, 1985; Yaziv, *et al.*, 1987). Data have also been reported for titanium diboride by Yaziv and Brar (1988). With the exception of these materials, little wave profile data have been reported for ceramics of interest as armor materials.

Although this report does not directly deal with ballistic impact, the wave profile data presented here can be used in the formulation and evaluation of material models to be implemented in wave propagation codes. The goals of such models include investigation of the mechanisms by which ceramics are able to defeat projectiles, and identification of important mechanical properties that contribute to performance. We recognize that plate impact data address only one regime of material response induced by projectile impact, and complementary dynamic studies (*e.g.* dynamic fracture and fragmentation) are needed to complete the dynamic data base of these materials.

Two-dimensional wave-code calculations have provided guidance on what regimes of strain rate need to be probed experimentally. For example, at distances of only one or two projectile diameters in front of the projectile tip, compressive and tensile loading rates are in the range of 10^3/s. Several rocks have exhibited strong correlations of fracture strength to strain rate imposed on the material (Grady and Lipkin, 1980),

and similar responses would not be surprising for ceramics. Diverging wave data are currently being generated that focus on the time-resolved particle motion on the back surface of ceramic targets impacted by 2 mm diameter projectiles (Wise and Cox, 1989).

The present report documents the response to plate impact of four ceramic materials for which wave profile data have been obtained: B_4C, SiC, TiB_2, and ZrO_2. Material characterization of the ceramics is discussed in Section 2, and a description of the uniaxial plate impact experimental methods employed in this study is the subject of Section 3. Section 4 is devoted to presenting experimental results, and Section 5 discusses techniques to recast the particle velocity data to *in-situ* stress-strain paths experienced by the ceramic targets. Section 6 contains comparisons of behavior for the ceramics in this study, and Section 7 is a summary of key results.

2. Materials

Three of the ceramics used in the present study (B_4C, SiC, and TiB_2) were stock obtained from the Los Alamos National Laboratory used in earlier armor studies, and for which little source information was available. The zirconium dioxide investigated in this suite of materials had reliable source information. The initial material characterization experiments at this laboratory determined ultrasonic longitudinal and shear wave speeds, C_L and C_S, and reference density, ρ_0, on all specimens. A summary of these experimental values is provided in Table 1. In addition, Table 1 includes elastic properties calculated from the measured density and ultrasonic wave speeds: bulk wave speed, C_0; Poisson ratio, ν; bulk modulus, K; shear modulus, μ; and longitudinal modulus, E_L. For reference, the equations relating these properties are listed below Table 1.

Table 1: Elastic Properties

Material	ρ_0 kg/m^3	C_L km/s	C_S km/s	C_0^* km/s	ν^*	K^* GPa	μ^* GPa	$E_L{}^*$ GPa
B_4C	2516	14.04	8.90	9.57	0.164	230.2	199.3	496.0
SiC	3177	12.06	7.67	8.19	0.160	212.9	186.9	462.1
TiB_2	4452	10.93	7.30	6.96	0.097	215.5	237.2	531.9
ZrO_2	5602	6.61	3.54	5.19	0.299	151.2	70.2	244.8

* Calculated quantities, according to the following:

$$\nu = \frac{C_L^2 - 2C_S^2}{2(C_L^2 - C_S^2)} \qquad C_0^2 = C_L^2 - \frac{4}{3}C_S^2$$
$$K = \rho_0 C_0^2 \qquad \mu = \frac{3K(1-2\nu)}{2(1+\nu)}$$
$$E_L = \rho_0 C_L^2$$

The partially stabilized zirconia (PSZ) used in the present experiments was obtained from McDonald Refractory, Beaver Falls, Pennsylvania. The material is 12.5 mol % yttria-doped zirconia with a density of 5602 kg/m^3. Properties reported by the manufacturer include a grain size of 7-15 μm, a Rockwell hardness of 68, a tensile strength of 140 MPa and a compressive strength greater than 1.7 GPa. A void fraction or porosity of 0.04 was measured for this zirconia.

Samples of all four ceramics were prepared through grinding, polishing, and etching to reveal the grain structure through optical microscopy. All samples showed fine grained, equiaxial grain structure. Specifically, nominal grain sizes of 7 μm, 12 μm, 10 μm, and 15 μm were obtained for the SiC, TiB_2, B_4C, and ZrO_2, respectively.

The same samples were used to perform electron probe microanalysis (EPMA) to determine elemental composition and microstructure characteristics. The titanium diboride studied was found to be quite clean of contaminants and close to TiB_2 stoichiometry. The EPM analysis revealed some porosity occurring principally at multiple grain boundary intersections, angular in geometry, and on the order of several percent. The zirconium dioxide studied was also found to be free of contaminants and near the

reported stoichiometry. Porosity was observed in the form of inter- and intragranular spherical pores. Silicon carbide investigated in this work was contaminated with inclusions principally of tungsten and tungsten carbide, but appreciable amounts of molybdenum, chromium, and titanium were also determined to be present. Porosity (about 1 %) in the form of near spherical cavities on grain boundaries was also observed. The boron carbide had significant iron contaminants occurring within voids and other sites distributed quite heterogeneously (relative to the grain size) throughout the material.

3. Experimental Method

Uniaxial strain compressive shock and release waves were produced in the ceramics of interest with a single stage powder gun facility. The gun used for these experiments has an 89 mm bore diameter and is capable of achieving a maximum impact velocity of 2.2 km/s. Three electrically shorting pins, as indicated in Figure 1, are used to measure the velocity of the projectile at impact. Four similar pins are mounted flush to the impact plane and used to monitor the planarity of impact. The pins are also used to trigger diagnostic equipment: the interferometer laser, various recording oscilloscopes, and transient digitizers. Projectile velocity can be measured with an accuracy of $\pm$ 0.5 % and the deviation from planarity of impact is typically about 10^{-3} radians.

A typical target configuration for the series of tests is shown in Figure 1. A disc of the ceramic being tested is mounted in the projectile and is supported on the main projectile body by a 7 mm thick disc of low density polyurethane foam. Both 20 and 40 pounds per cubic foot (320 and 640 kg/m^3) foam were used in the present study. An aluminum ring encloses the ceramic disc as shown and provides a metal surface for electrically shorting the various diagnostic pins.

For the target, a similar disc of the ceramic is mounted in the stationary supporting ring. An optical quality single crystal of lithium fluoride in the shape of a disc 50 mm in diameter and 25 mm thick is intimately bonded with epoxy to the back of this ceramic

sample. All critical surfaces are lapped and polished, and are typically flat to within a few bands of sodium light. The bonded lithium fluoride surface is first lightly diffused and vapor-deposited with about 1000 Angstroms of aluminum. The ceramic-lithium fluoride epoxy bond thickness is approximately 10 to 20 μm.

The ceramic-on-ceramic planar impact produces a compressive wave of uniaxial strain which propagates through the stationary ceramic specimen and through the ceramic-lithium fluoride interface. An equivalent compressive wave propagates through the projectile ceramic specimen and reflects at the low-impedance foam interface as a release wave which unloads the compressed ceramic. Dimensions of the ceramic discs are selected such that release waves from the boundaries of the disc do not interfere with the central motion until after the experimental measurement is completed.

The compression and release wave behavior is measured by monitoring the time-resolved longitudinal motion of the ceramic-lithium fluoride interface with laser velocity interferometry (VISAR) techniques (Barker and Hollenbach, 1972). Measurements are recorded on transient digitizers with a sampling period of 0.742 ns per data point. Lithium fluoride is used as the laser window material because, although its mechanical impedance is somewhat lower than the ceramics being tested, it is the only material which has been optically calibrated and which remains transparent when subjected to the 30 to 40 GPa shock stresses generated in the present experiments (Wise and Chhabildas, 1986).

The interference fringes measured with the VISAR system are converted to a time-resolved history of the velocity of the interface using the method of Barker and Hollenbach (1972), with a resolution of approximately 1 ns. From these records the dynamic stress and strain characteristics of the ceramics are determined through further analytic techniques which are described in a later section.

4. Experimental Results

Two experiments each were performed on the four materials investigated. Impact conditions were selected to achieve maximum axial stress states of order two to four times the Hugoniot elastic limit of the materials. Thus, maximum stress states near 50 GPa were achieved in some cases. With the exception of the TiB_2, projectile and target plate thicknesses within each pair are similar, thus minimizing geometry effects when comparing records. The impact velocity and experimental dimensions pertinent to each test are provided in Table 2.

Table 2: Experimental Conditions for Ceramic Impact Tests

Test No.	Material	Impact Velocity (km/s)	Foam Density (kg/m^3)	Impactor Thickness (mm)	Target Thickness (mm)
1	B_4C	1.546	320	3.920	9.044
2	B_4C	2.210	640	3.917	9.033
3	SiC	1.542	320	3.987	8.939
4	SiC	2.100	640	3.995	8.940
5	TiB_2	1.515	320	3.972	10.804
6	TiB_2	2.113	640	3.337	10.747
7	ZrO_2	1.556	320	3.313	6.635
8	ZrO_2	2.075	640	3.247	6.324

Time-resolved velocity profiles corresponding to the interface motion identified in the experimental configuration (Figure 1) are displayed in Figures 2 - 5. Each record consists of about 1500 digitized data points. The erratic excursions in the B_4C velocity histories are accurate records of the local material motion, and not the result of faulty instrumentation. These records will be discussed in detail later. However, even a cursory comparison of the profiles for these four ceramics suggests that very diverse behavior is represented by these materials. The arrival times of the wave profiles are arbitrary and were selected to offset and display the records. Actual transit times through the target specimen should be calculated from the specimen thickness and

the initial transit wave velocity. The latter was measured in each test but within experimental accuracy could not be distinguished from the corresponding longitudinal velocity reported in Table 1.

The records shown in Figures 2 - 5 qualitatively illustrate the evolution of the compression and release wave caused by the initial impact and subsequent unloading due to wave reflection at the foam-ceramic interface. The profile is distorted somewhat in both amplitude and shape, however, due to the mechanical impedance difference between the lithium fluoride and ceramic. Impedance matching techniques were used to extract some yield information from the profiles. A more detailed analysis of the data to infer properties relating to the stress-strain behavior of the ceramics relied on computational techniques that are described in the following section.

5. Dynamic Compression and Release Properties

Additional insight into the ceramic response to shock loading is gained by transforming the particle velocity history into a stress-strain load-release curve for each experiment. As noted earlier, the lithium fluoride window is not a perfect impedance match to the ceramic target, so that when a wave is transmitted into the window from the ceramic, reflections occur at the contact interface. The measured particle velocity profile at this interface includes the complications of these reflections. One very important reason for making the transformation from the particle velocity history to a stress-strain path is to separate features in the measured wave profiles associated with wave interactions caused by the sample and window material impedance mismatch from features associated with material response properties of the ceramics (yield, phase transformations, *etc.*). An understanding of the material response interior to the target ceramic also provides a means for determining more clearly the elements necessary to model these materials. In all cases, the analysis was accomplished using the one-dimensional explicit Lagrangian shock wave propagation code, WONDY (Kipp

and Lawrence, 1982).

Standard material models (*e.g.* elastic-perfectly plastic, strain-hardening plasticity) using ultrasonically-determined reference values and Hugoniot data from Gust and Royce (1971) and Gust, *et al.* (1973) were initially used for each material. Of the four ceramics, only SiC could be readily represented with an elastic-perfectly plastic model. A much better fit for SiC was made with a traditional strain-hardening model which, for a single set of parameters, captured nearly all of its load and release response. For the other three ceramics in this study, the limitations of the elastic-perfectly plastic assumptions were to be found primarily in the inability to accommodate the very dispersive nature of the unloading wave that first forms in the projectile ceramic, then propagates through the target to the window.

In order to obtain accurate internal stress-strain histories, a technique patterned after that developed by Grady and Furnish (1988) was used, in which a parameterized load-unload path was incorporated into WONDY, and exercised in an iterative fashion. In each WONDY iteration, spline-fit points defined loading and unloading paths that were adjusted for the ceramic until the VISAR interface particle velocity history was reproduced. The parameters determined in this way typically are only unique to a particular experiment, not to the material. It should be noted here that we have assumed that the primary contribution to the stress is the material strain, and dependence on both strain rate or thermal effects has been neglected. Hence, any model development based on these data should use the particle velocity histories as the final basis of comparison. In some tests, high release velocities result in erosion or attenuation of the shock by the release wave. In the analysis, this required the release path to be referenced to the maximum local stress state. This "floating" reference point in the ceramic is saved, and the start of the release path referenced to that state. Ultrasonic data were used to define the initial loading moduli. After each experiment has been matched, stress-strain histories interior to the ceramic are readily found, and moduli can be determined by differentiating the path. The stress-strain paths that are plotted subsequently contain only the mechanical response, and *do not* include the artificial

viscous stress used in WONDY to treat problems involving shock wave propagation.

This technique provides an estimate of the Hugoniot elastic limit for each material, as well as insight into the energy dissipated in the material in a load-release cycle, some measure of residual strength, and fracture properties. The materials will first be discussed individually in this section, and then some comparative comments will be made in the following section.

Silicon Carbide

Only in the case of SiC could the particle velocity profiles be reproduced with a simple material model. Herrmann's strain-hardening model in WONDY (Herrmann, *et al.*, 1970; Kipp and Lawrence, 1982), originally formulated to account for metal plasticity, uses a piecewise continuous curve of stress-strain pairs to describe the smooth transition between the elastic precursor and the second plastic wave. The reference bulk and deviatoric properties are based on the measured ultrasonic parameters and a linear $U_S - u_P$ Hugoniot (Gust and Royce, 1971) with $s = 1$. As is readily apparent in Figures 6 and 7, the parameters used in the model lead to calculated particle velocity profiles that are in very good agreement with the experimental data. Appendix A includes the WONDY input data for the low amplitude case (1.54 km/s impact velocity). The additional disturbance in the structure of the second wave in the 2.1 km/s case (Figure 7) is a result of precursor and secondary wave interactions at the target/window interface. Most remarkable is the apparent full retention of yield strength exhibited by the SiC during and after unloading. It was necessary to include a fracture strength of 50 MPa in the calculation to maintain the particle velocity at late times. If fracture is suppressed in the calculation, then a sudden drop in particle velocity occurs just after 1.3 μs. Both the high and low amplitude calculations used the same model parameters. After 1.4 μs, the wave shows evidence of dispersion at low amplitudes, suggesting that some material fracture has occurred.

If this ceramic material behaved in a classic elastic-perfectly plastic manner, a

representative load-release path at a position in the target material in uniaxial strain would have the appearance of the path plotted in Figure 8. The reference hydrostat is included in the plot. The load path is elastic to the Hugoniot elastic limit, where a break in the curve occurs at the intersection with the yield surface, and loading continues on the yield surface, maintaining a separation from the hydrostat of two-thirds the yield strength. When unloading commences, the material releases elastically, crosses the hydrostat, and again intersects the yield surface, and further unloading is on the yield surface. The paths are characterized by sharp transitions from elastic to plastic states.

The strain hardening model, in contrast, smooths the transition from elastic to plastic states, as seen in the load-release paths in Figure 9, monitored at the midpoint of the ceramic targets. The paths for the low and high amplitude experiments overlay one another to the onset of unloading for the low amplitude experiment (28 GPa). At this point, the low amplitude experiment unloads elastically past the hydrostat, eventually into a tensile state. In the high amplitude case, a compressive stress of about 36 GPa is achieved before unloading. When the path is below the hydrostat, the strain hardening character is observed to reappear at the conclusion of the elastic unloading phase (Compare with Figure 8). In these loading paths, the curvature in both the elastic and yielding parts supports shock waves except during the hardening portion of the loading. For reference the hydrostat used in the calculation appears on the plot. In addition, Hugoniot data acquired by Gust, *et al.* (1973) for their SiC are included in Figure 9, and, apart from being considerably more scattered than the current data, fall well below the loading path determined from the present experiments. Note in particular the significantly higher Hugoniot elastic limit implied by the present data compared to that of Gust, *et al.* (1973). The previous values for a Hugoniot elastic limit for SiC are plotted in Figure 10, along with the values obtained in the present work (see Table 3). The current value inferred from the computational analysis is nearly 16 GPa, and independent of pressure, whereas previous data tend to be rather scattered, and hint of pressure dependence. The possible contribution of porosity or

fabrication techniques to these yield differences is difficult to ascertain.

Silicon carbide was one of the strongest ceramics tested (comparable with boron carbide) with a measured Hugoniot elastic limit of approximately 15 GPa. This value is approximately twice that reported by Gust, *et al.* (1973) on a slightly lower density silicon carbide. In addition, silicon carbide exhibited dynamic hardening characteristics following initial yield which significantly increased the effective flow stress. The shock compression and release experiments on silicon carbide provided the only wave profile measurements which were adequately predicted with a standard work-hardening elastic-plastic material response model. This was because the silicon carbide did not exhibit the large release wave dispersion observed for the other materials. The reasons for this are, as yet, unclear since underlying mechanisms for this anomalous dispersion are not yet known. Some possible mechanisms are discussed in the next section. Gust, *et al.* (1973) infer a possible phase change in silicon carbide at about 25 GPa from a discontinuity in Hugoniot data. Although the present profiles do not provide a clear indication of such a transformation on compression, the observed small amount of dispersion on release could imply reverse phase change through a tendency to support a rarefaction shock wave.

Boron Carbide

This material has a very high longitudinal wave velocity, with the result that for the projectile and target plate thicknesses in these experiments, attenuation of the initial shock by the unloading wave begins to occur before the shock has reached the target/window interface. The unloading wave is much more dispersive than could be modeled by the curvature of a solid hydrostat based on the data of Gust and Royce (1971). In addition the second loading wave is also dispersive for both amplitudes. Iteration on loading and unloading parameters converged to the sets that provide the fits shown in Figures 11 and 12. The amplitude of the elastic precursor was chosen in these cases to correspond to an average amplitude. If a higher value for yield is chosen,

in order to capture the peak seen in the data, then a noticeable shift in the plateau in the release wave at 1.5 μs (in the 1.55 km/s case) is observed. These fits do not capture the apparent loss of strength just beyond initial yield, nor the chaotic behavior of the material in general. We are not yet able to provide a satisfactory explanation for the disappearance of the peak in the experimental record in the low amplitude experimental data (Figure 11).

A plot of the calculated stress-strain paths in the center of the B_4C target is given in Figure 13. Again, previous Hugoniot data (Gust and Royce, 1971) are included in the Figure, and are in very good agreement with the current data. We notice that the curve labelled "EPP", calculated assuming elastic-perfectly plastic behavior based on ultrasonic measurements, is more stiff at the transition to yield than the actual response. We conclude that the B_4C is experiencing a reduction in strength above the Hugoniot elastic limit. The downward curvature during yield reflects the dispersion seen on the second loading wave. Upon unloading from both amplitudes, there is a complete change in character from any evidence of explicit yield behavior. The large curvature is necessary to obtain the wide dispersion seen in the interface particle velocity records. The curvature in this unloading path is much greater than could normally be associated with hydrostatic response, and hence, cannot readily be attributed to material exhibiting complete loss of shear strength.

A reasonable approach for determining a reference hydrostat for B_4C is to use only the highest pressure Hugoniot data from Gust and Royce (1971), assuming that material strength effects are unchanging at these pressures, and the ultrasonic data from Table 1. Then a linear $U_S - u_P$ relation fits the data with an s of 1.

The boron carbide wave profiles show a well-defined compressive elastic limit but are unique in the chaotic particle velocity observed. This behavior has been observed previously in VISAR measurements on single-crystal olivine (Furnish, *et al.*, 1986). The erratic motion has been attributed to a heterogeneous failure or faulting mechanism during compressive loading coupled with the small laser spot size associated with

VISAR measurements. The characteristic period of the chaotic motion would suggest heterogeneous faulting on a scale of 0.5-1.0 mm. The Hugoniot elastic limit of B_4C is comparable to that of SiC and is in agreement with earlier work of Gust, *et al.* (1973). As noted previously, the slow plastic wave speed is consistent with partial loss of strength at the Hugoniot state. The dispersive release wave behavior is consistent with that observed in TiB_2 and ZrO_2.

Titanium Diboride

The calculated particle velocity profiles for the TiB_2 are shown in Figures 14 (low amplitude) and 15 (high amplitude). The most striking feature of the low amplitude profile is the considerable dispersion of the loading wave profile that is apparent (Figure 14). The calculated stress-strain paths in the center of the target are plotted in Figure 16, along with the Hugoniot data of Gust, *et al.* (1973). The risetime of 0.4 μs to 1 km/s (32 GPa) in the lower amplitude experiment is interrupted by two breaks, the larger of which occurs at 0.42 km/s (13.7 GPa). The wave profile in the higher amplitude experiment has a finite risetime below 13.7 GPa, and forms a shock above 13.7 GPa. In both cases, as in the B_4C, the release wave is dispersive. The stress strain plots indicate that there is no discrete yield behavior during release. During loading, the higher amplitude stress strain plot shows the large upward curvature required for shocks to form. There is general agreement between the data of Gust, *et al.* (1973) and the current data below 35 GPa, although the continuous curvature of the release stress strain path is far greater than that of the Hugoniot from Gust, *et al.* (1973). This implies that the material has an unloading structure more complex than simple elastic plastic response.

The titanium diboride experimental profiles shown in Figure 4 are uniquely characterized by the large risetime, or ramp-wave structure, of the compressive wave. The dispersion of an initial compressive shock wave to a ramp wave at pressures approaching 50 GPa is quite unusual. The structuring mechanism is not known and further

tests will be required to determine whether the structured shocks are unsteady or have steady components. In contrast to the profiles measured on the other ceramics in this series of tests, it is difficult to identify an unambiguous break in the compressive wave which corresponds to the onset of compressive yield. From expanded plots of the compressive wave, breaks at particle velocity levels of approximately 0.16 and 0.42 km/s were observed which correspond to stresses of about 5 and 13 GPa, respectively. We have tentatively identified the first break with complexities in the plastic flow or to a phase transformation. We identify the second break with the Hugoniot elastic limit for TiB_2. The wave velocity following the second break is approximately the bulk wave velocity, which is consistent with conventional elastic-plastic behavior. Values of the Hugoniot elastic limit reported by Yaziv and Brar (1988) range from 7.1 to 7.9 GPa for titanium diboride.

The release wave profile of TiB_2 contrasts sharply with the behavior of SiC in that a broadly dispersing release wave or a wave with rapidly decreasing wave velocity with decreasing stress was measured. Similar behavior was observed in B_4C and ZrO_2. Such wave propagation behavior is impossible to predict with conventional elastic-plastic models.

Zirconium Dioxide

For the ZrO_2 impact data, the loading displays a character that is very similar to that of the SiC (*i.e.* strain hardening), as seen in Figures 17 and 18. But the dispersive unloading suggests that there has been a substantial loss in strength resulting from the loading process. Nonetheless, the material still has retained a non-zero fracture stress. The calculations that gave the fit required a fracture stress of less than 100 MPa in order to maintain the velocity amplitude of the trailing tail. Figure 19 indicates the particle velocity that is obtained in a calculation in which the ZrO_2 was not permitted to fracture - a precipitous decrease in particle velocity is then observed. The stress-strain paths for these configurations are shown in Figure 20, in which the dispersive character

of the loading wave transition above the HEL is apparent, as is the continuously curved unloading path, required to disperse the wave during release. The stiffness of ZrO_2 is clearly much less than that of the other three ceramics in this study, and at these impact velocities supports very large strains.

The zirconium dioxide tested in the present study provided a distinct two-wave compressive structure very similar to that of silicon carbide. An initial Hugoniot elastic limit of about 5 GPa is followed by a dynamic hardening region and a short risetime deformational shock wave. Zirconia in the presence of small amounts of other oxides (yttria, calcia, magnesia) is known to exist in several pressure sensitive polymorphs. There is no evidence for a pressure-induced phase transformation in the present shock and release wave profile, however. The present material differs from that tested by Mashimo, *et al.* (1983) which was crystalline zirconia in the monoclinic phase and in which no clear elastic precursor was detected. It also differs from further work reported by Mashimo (1988) on calcia-stabilized sintered zirconia with a Hugoniot elastic limit of 6.8-9.2 GPa and partially stabilized yttria-doped zirconia with an unusually high Hugoniot elastic limit of 35-39 GPa (Mashimo, 1988). The present fully stabilized yttria-doped zirconia (HEL = 5.0-5.4 GPa) failed to provide dynamic strengths consistent with these latter values. Although some porosity in our specimens may account for part of this difference, it is suspected that microstructural details of the partial stabilization process play a major role in the dynamic strength of this material.

6. Discussion

In the present exploratory study of the shock compression and release properties of ceramics, a number of unusual features were uncovered which attest to the unique and complex failure and flow characteristics of these materials. In the current section we attempt to identify some common trends relating to the dynamic yield and deformation characteristics of the set of ceramics investigated.

Hugoniot Elastic Limit

For the comparative analysis in this section, the Hugoniot elastic limits for the various ceramics tested were determined directly from the measured particle velocity profiles (Figures 2-5) accounting for the impedance mismatch between ceramic and window. The expression used was $\sigma_{HEL} = \frac{Z_C+Z_L}{2} u_M$ where Z_C and Z_L are the appropriate shock impedance for the ceramic and lithium fluoride, respectively, and u_M is the observed particle velocity amplitude selected from each profile which represents the transition from elastic to nonelastic behavior. For the ceramic $Z_C = \rho_0 C_L$, since as was noted earlier, within experimental uncertainty, the finite amplitude elastic velocities and ultrasonic velocities were the same. For lithium fluoride $Z_L = \rho_0(C_0 + s u_M)$ with $\rho_0 = 2641$ kg/m^3, $C_0 = 5148$ m/s, and $s = 1.353$.

The Hugoniot elastic limit data (σ_{HEL}) are tabulated in Table 3 and displayed in Figure 21 as a function of peak wave amplitude (Hugoniot stress, P_H). For silicon carbide the initial break from the steeply rising initial wave to the ramping region above this wave was chosen for u_M. For boron carbide u_M was determined from the somewhat noisy plateau region between the first and second wave. The structure of the compressive wave for titanium diboride caused difficulty in unambiguously selecting a particle velocity corresponding to the HEL. A reasonably well-defined break in both waves at approximately 160 m/s was tentatively selected as a preliminary yield process or phase transformation u_M value. There is a second, major, break at about 420 m/s, however, which is also a consequence of some structuring feature in the TiB_2 material response, and is presumed to be the Hugoniot elastic limit. This is also identified in Table 3 and Figure 21. The appropriate u_M for zirconium dioxide was determined from the break between steep and ramped wave behavior.

Table 3

Test No.	Material	u_M (m/s)	σ_{HEL} (GPa)	P_H (GPa)
1	B_4C	580±30	14.8	22.8
2	B_4C	550±40	14.0	31.4
3	SiC	550±30	14.8	27.6
4	SiC	570±30	15.3	36.5
5	TiB_2	165±15	5.2	31.0
"	"	430±40	13.7*	"
6	TiB_2	150±15	4.7	48.5
"	"	410±20	13.1*	"
7	ZrO_2	195±10	5.0	23.6
8	ZrO_2	210±10	5.4	33.2

* Corresponds to second yield structure in TiB_2

Yield Behavior

The Hugoniot elastic limit identifies the limits of elastic response in a dynamic (shock-wave) uniaxial strain loading. Subsequent response is governed by the yield and post-yield response of the material. In many shock-wave studies it is common to assume a von Mises condition of yield which asserts that yield initiates when the second deviatoric stress invariant attains a critical value. Through this formalism the yield stress in simple tension, Y, can be easily related to the HEL through,

$$Y = 2\frac{C_S^2}{C_L^2}\sigma_{HEL}. \tag{1}$$

Yield stress values calculated in this way for the high-strength ceramics investigated in the present study are tabulated in Table 4 under $Y(Stress)$ and plotted in Figure 22 as a function of reference shear modulus (Table 1). Several methods have been used to calculate the theoretical shear strength, τ_{TH}, of perfect crystals, which result in values ranging over $G/5 \geq \tau_{TH} \geq G/30$ (Heirth and Lothe, 1968). Assuming $\tau_{TH} = G/15$ and using the relation $Y = \sqrt{3}\tau$, a curve for the threshold value of $Y(Theoretical)$ is

provided for reference in Figure 22 and tabulated in Table 4, based on the zero-pressure value of the shear modulus.

Table 4

Material	σ_{HEL} (GPa)	$Y(Stress)$ (GPa)	$Y(Theoretical)$ (GPa)
B_4C	14.0-14.8	11.3-11.9	23.0
SiC	14.8-15.3	12.0-12.4	21.5
TiB_2	4.7-5.2	4.2-4.6	27.4
"	(13.1-13.7)*	(11.7-12.2)	
ZrO_2	5.0-5.5	2.9-3.1	8.1

* Corresponds to second yield structure in TiB_2

For SiC and ZrO_2 clear evidence of deformation hardening following initial yield at the HEL is observed in the measured wave profile. The approximate magnitude of this hardening is indicated in Figure 22.

Compressive Wave Risetime

A unique feature of the present time-resolved wave profiles was the ability of VISAR instrumentation to resolve the risetime of the compressive deformational shock wave in these materials. (The deformational shock wave refers to the slower structural wave following the elastic precursor wave which carries the material up to the peak, or Hugoniot, stress.) In metals, this wave cannot be resolved with the approximately one nanosecond resolution of the VISAR system at comparable peak stress levels.

It is important to caution the reader that complex wave interactions associated with the elastic precursor wave and the impedance mismatch at the lithium fluoride window can lead to fictitious risetime effects. These details have been worked out for a free surface (Grady, 1986) but have not yet been treated for the present case. Consequently, the present risetime data and observations should be regarded as very preliminary.

We plot the data in the form shown in Figure 23. The pressure step on the ordinate refers to the amplitude of the deformational shock wave. Errors in this property are principally determined by the uncertainty in selecting the breakaway of this wave above the HEL. The strain rate on the abscissa is determined from the maximum velocity rate measured in the deformational shock wave and the shock velocity of this wave. The data are compared with the quarter-power behavior observed in other materials (Swegle and Grady, 1985).

We note in passing a tentative correlation between the magnitude of the HEL and the width of the deformational wave in comparing the behavior of ceramics and metals. Also B_4C and SiC, the ceramics in the present study with the highest HEL's, exhibit somewhat steeper slopes in Figure 23. This is not unlike the behavior of uranium for peak stress within a factor of 2 to 3 times the HEL value (Grady, 1986).

Comparison of Load-Release Paths

Load-release paths for the four ceramics are compared in Figures 24 and 25. The paths resulting from the low-amplitude calculations are shown in Figure 24, and the higher amplitude ones in Figure 25. Note that although there is almost a factor of two spread in densities, the elastic loading curves of B_4C, SiC, and TiB_2 are very nearly identical in both low and high amplitude cases. However, in the low amplitude case, the TiB_2 clearly dissipates more energy than the other two (based on similar impact velocities). The B_4C shows a major loss in strength when compared to the other two ceramics. Although the SiC and TiB_2 respond similarly in the low amplitude impact, at the higher impact velocities, the TiB_2 is stiffer than either of the other two, with the B_4C still being the weakest of these three. Note that in the latter case, the SiC dissipates the most energy.

7. Conclusions

The present set of eight experiments on silicon carbide, boron carbide, titanium diboride, and zirconium dioxide provide an overview of the wide range of possible response of ceramics to dynamic compressive loading and release. The large yield strengths associated with ceramics are verified. The titanium diboride exhibits significant dispersion of compression waves to 50 GPa. The boron carbide, titanium diboride, and zirconium dioxide disperse the release waves more widely than normal solid response should be, suggesting internal damage during compression has altered the state of the material. Only silicon carbide exhibits traditional elastic-strain hardening-plastic response to shock loading. The continuous load-release curves provide a substantial database for evaluating computational models.

The next stage of the program will include construction of a model that can describe the dynamic responses observed in the present experimental study, as well as continuation of impact equation of state experiments. Further areas of investigation need to include shock compression and release to lower amplitudes than possible here, propagation distance evolution of the shock, initial shock-amplitude dependence of spall, strain-rate dependence of spall, and ramp load and release.

8. Acknowledgement

This work on Advanced Armor / Anti-Armor Materials was funded by the Balanced Technology Initiative through both the Defense Advanced Research Projects Administration and the Army Research Office.

9. References

T. J. Ahrens, W. H. Gust, and E. B. Royce (1968) "Material Strength Effect in the Shock Compression of Alumina", *Journal of Applied Physics*, **39**, 10, 4610-4616.

L. M. Barker and R. E. Hollenbach (1972) "Laser Interferometer for Measuring High Velocities of Any Reflecting Surface", *Journal of Applied Physics*, **43**, 11, 4669-4675.

J. Cagnoux and F. Longy (1988) "Spallation and Shock-Wave Behavior of Some Ceramics", *Journal de Physique*, Colloque C3, **49**, 3-10.

M. D. Furnish, D. E. Grady, and J. M. Brown (1986) "Analysis of Shock-Wave Structure in Single Crystal Olivine Using VISAR", in Shock Waves in Condensed Matter, Y. M. Gupta, Ed., Plenum, New York, 595-600.

D. E. Grady and J. Lipkin (1980) "Criteria for Impulsive Rock Fracture", *Geophysical Research Letters*, **7**, 255-258.

D. E. Grady (1986) "Steady-Wave Risetime and Spall Measurements on Uranium (3-15 GPa)", in Metallurgical Applications of Shock-Wave and High-Strain-Rate Phenomena (L. E. Murr, K. P. Staudhammer, M. A. Meyers, eds.) Marcell Decker, New York, 763-780.

D. E. Grady and M. D. Furnish (1988) "Shock- and Release-Wave Properties of MJ-2 Grout", Sandia National Laboratories Report SAND88-1642, December 1988.

W. H. Gust and E. B. Royce (1971) "Dynamic Yield Strengths of B_4C, BeO, and Al_2O_3 Ceramics", *Journal of Applied Physics*, **42**, 1, 276-294.

W. H. Gust, A. C. Holt, and E. B. Royce (1973) "Dynamic Yield, Compressional, and Elastic Parameters for Several Lightweight Intermetallic Compounds", *Journal of Applied Physics*, **44**, 2, 550-560.

J. P. Heirth and J. Lothe (1968) "Theory of Dislocations", McGraw-Hill, New York, 6-8.

W. Herrmann, R. J. Lawrence, and D. S. Mason (1970) "Strain Hardening and Strain Rate in One-Dimensional Wave Propagation Calculations", Sandia Laboratories Report SC-RR-70-471, November 1970.

M. E. Kipp and R. J. Lawrence (1982) "WONDY V - A One-Dimensional Finite-Difference Wave Propagation Code", Sandia National Laboratories Report SAND81-0930, June 1982.

T. Mashimo, K. Nagayama, and A. Sawaoka (1983) "Shock Compression of Zirconia ZrO_2 and Zircon $ZrSiO_4$ in the Pressure Range up to 150 GPa", *Physics and Chemistry of Minerals*, **9**, 237-247.

T. Mashimo (1988) "Anomalously High Hugoniot-Elastic Limit (35-39 GPa) of Y_2O_3-Doped Partially Stabilized Zirconia Ceramics", *Journal of Applied Physics*, **63**, 9, 4747-4748.

D. E. Munson and R. J. Lawrence (1979) "Dynamic Deformation of Polycrystalline Alumina", *Journal of Applied Physics*, **50**, 10, 6272-6282.

Z. Rosenberg (1985) "Dynamic Uniaxial Stress Experiments on Alumina with In-Material Manganin Gauges", *Journal of Applied Physics*, **57**, 11, 5087-5088.

J. W. Swegle and D. E. Grady (1985) "Shock Viscosity and the Prediction of Shock Wave Risetimes", *Journal of Applied Physics*, **58**, 692-701.

D. Viechnicki, W. Blumenthal, M. Slavin, C. Tracy, and H. Skeele (1987) "Armor Ceramics - 1987", Proceedings Third Tacom Armor Coordinating Conference 17-19 February 1987, Monterey, California.

M. L. Wilkins, C. F. Cline, and C. A. Honodel (1969) "Light Armor", Lawrence Radiation Laboratory Report UCRL-71817, July 1969.

J. L. Wise and L. C. Chhabildas (1986) "Laser Interferometer Measurements of Refractive Index in Shock-Compressed Materials", in *Shock Waves in Condensed Matter*, Edited by Y. M. Gupta, Plenum (1986) 441-454.

J. L. Wise and D. E. Cox (1989) "Initial Time-Resolved Measurements of Ballistic Penetrator Response for Ceramic (TiB_2) and Steel Plates", Sandia National Laboratories Memorandum to M. E. Kipp and P. Yarrington, Division 1533, February 21, 1989.

D. Yaziv, Y. Yeshurun, Y. Partom, and Z. Rosenberg (1987) "Shock Structure and Precursor Decay in Commercial Alumina", in *Shock Waves in Condensed Matter 1987*, Edited by S. C. Schmidt, N. C. Holmes, Elsevier (1988), 297-300.

D. Yaziv and N. S. Brar (1988) "Shock Wave Study of Titanium Diboride", *Journal de Physique*, Colloque C3, 49, 683-687.

10. Appendix A

```
 1     FOAM/4MM SIC/9MM SIC/LIF (1.54KM/S)(CE4)(0.5KB SPALL)
 2          1    4   20    3    3  300    1          1  180
 3          2.E-06    1.0E-9  -1.0E+06   1.0E+06 -0.013987
 4         0.9                                              1.0E30
 5         0.0       1.0E-06   1.0
 6         0.0       1.0E-08   1.0
10    1    1.0      200.0        0.01      0.00005   0.00005
12    1                                        1542.0    1542.0
14    1    2.0       -1.0E+06
15    1    320.0    1000.0
16    1    0.0                1.33
17    1    1.0       1.00
10    2    4.0       80.0      0.003987    0.00005   0.00005
12    2                                        1542.0     771.0
14    2    2.0       -1.0E+06
15    2   3177.0     8186.0                                0.160
16    2    0.0        1.0        1.0        1.0                0.0       -
6.0
17    2    130.0E8    145.0E8    160.0E8    170.0E8    190.0E8    200.0E8
18    2    0.307      0.231      0.152      0.076      0.115      0.115
10    3    4.0       180.0      0.008939    0.00005   0.00005
13    3    2.0         -0.5E8
14    3    2.0         -1.0E6
15    3   3177.0     8186.0                                0.160
16    3    0.0        1.0        1.0        1.0                0.0       -
6.0
17    3    130.0E8    145.0E8    160.0E8    170.0E8    190.0E8    200.0E8
18    3    0.307      0.231      0.152      0.076      0.115      0.115
```

```
10    4   1.0     500.0       0.025       0.00005   0.00005
15    4  2641.0   5148.0
16    4   0.0                   1.353
17    4   1.0       1.5
```

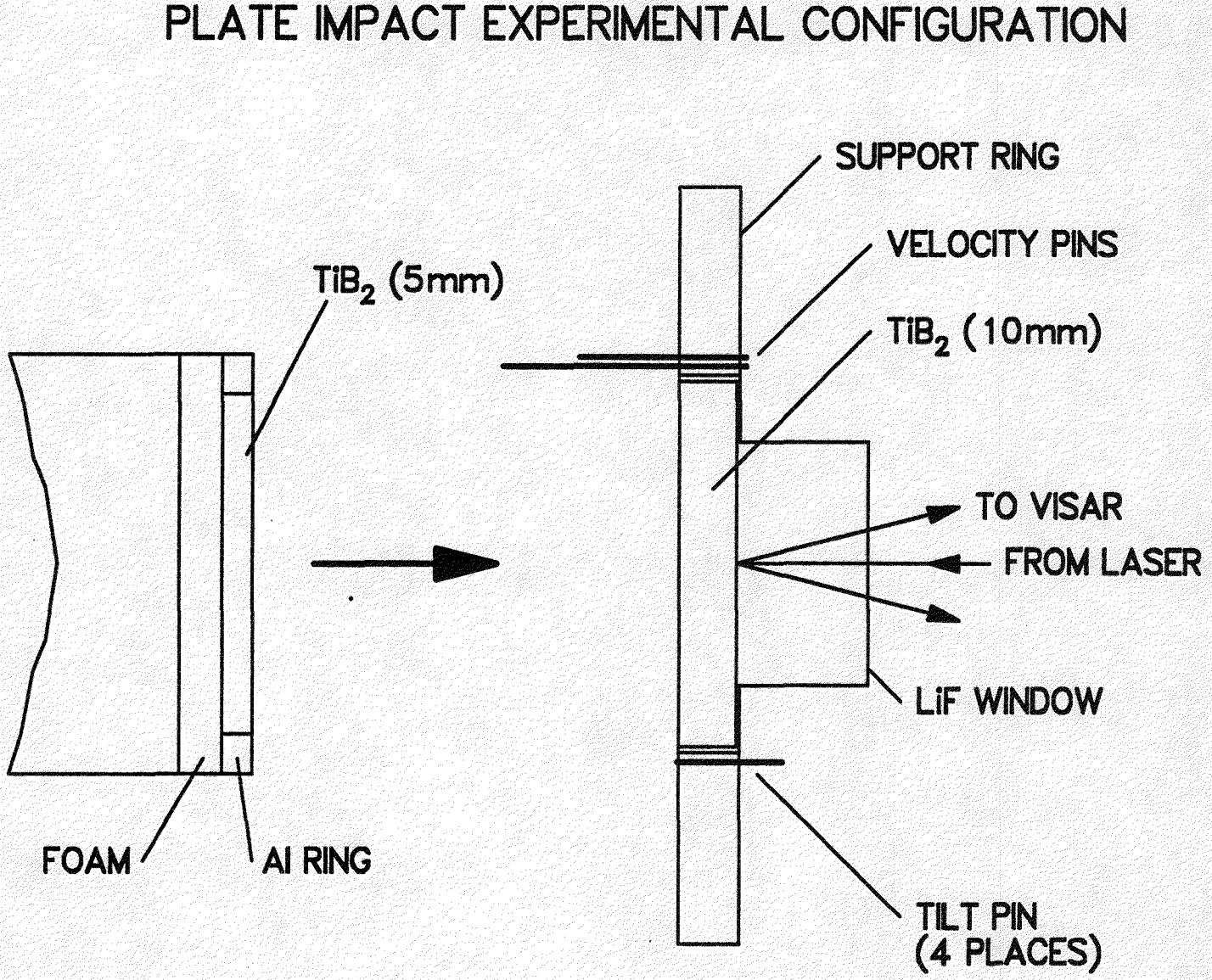

Figure 1: Plate impact experimental configuration.

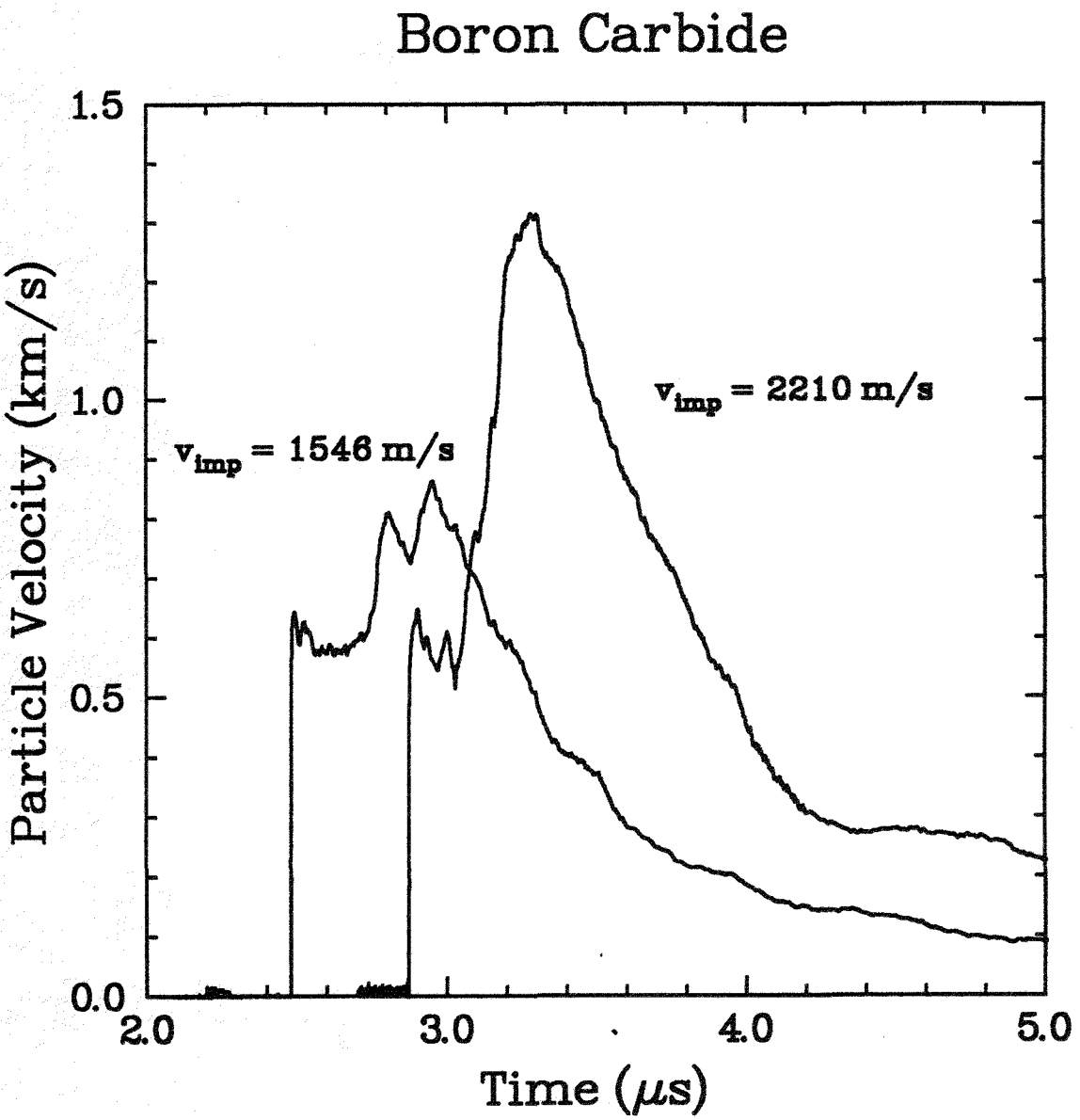

Figure 2: Boron carbide particle velocity histories for 1.5 and 2.2 km/s symmetric plate impact velocities.

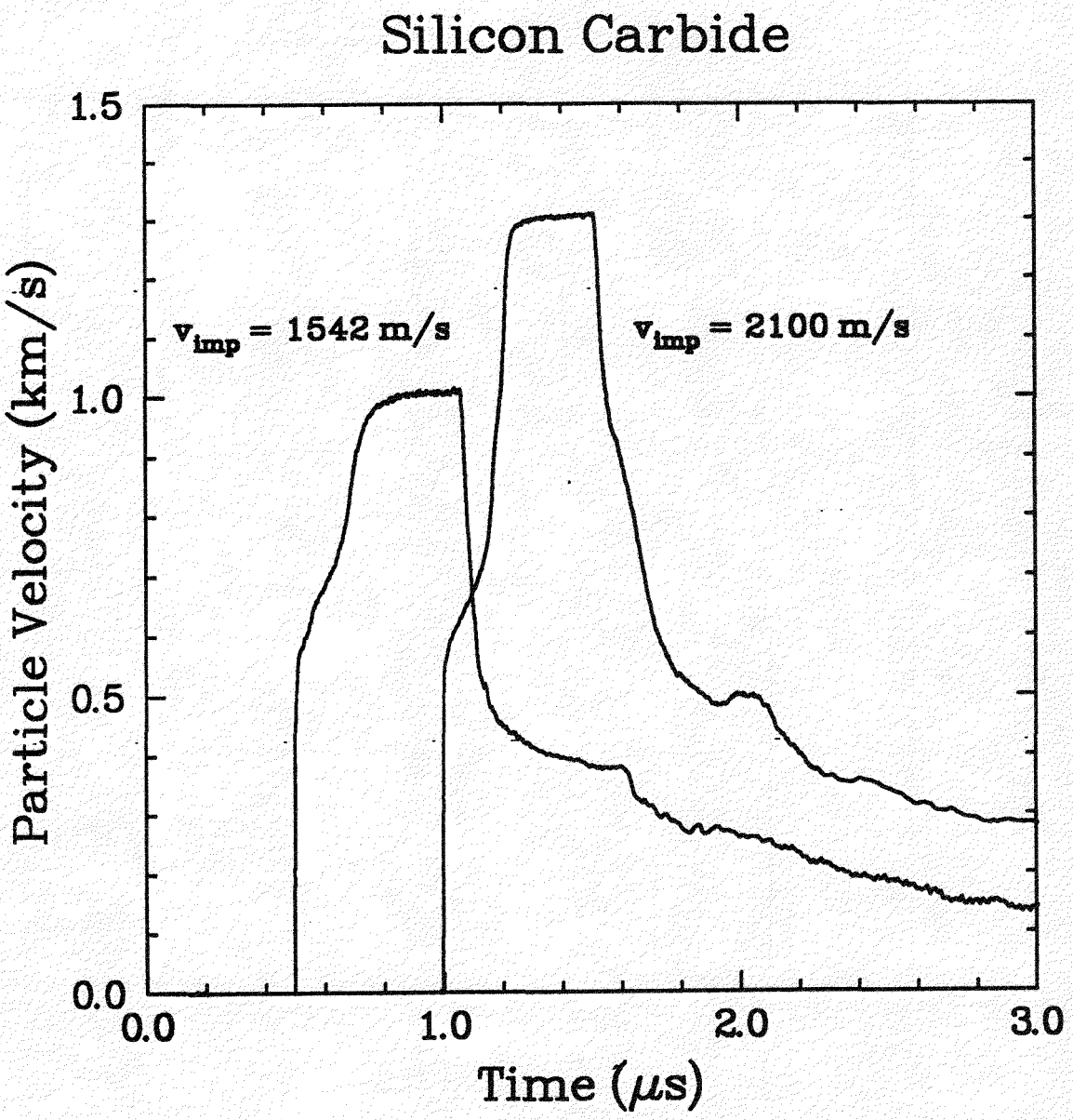

Figure 3: Silicon carbide particle velocity histories for 1.5 and 2.1 km/s symmetric plate impact velocities.

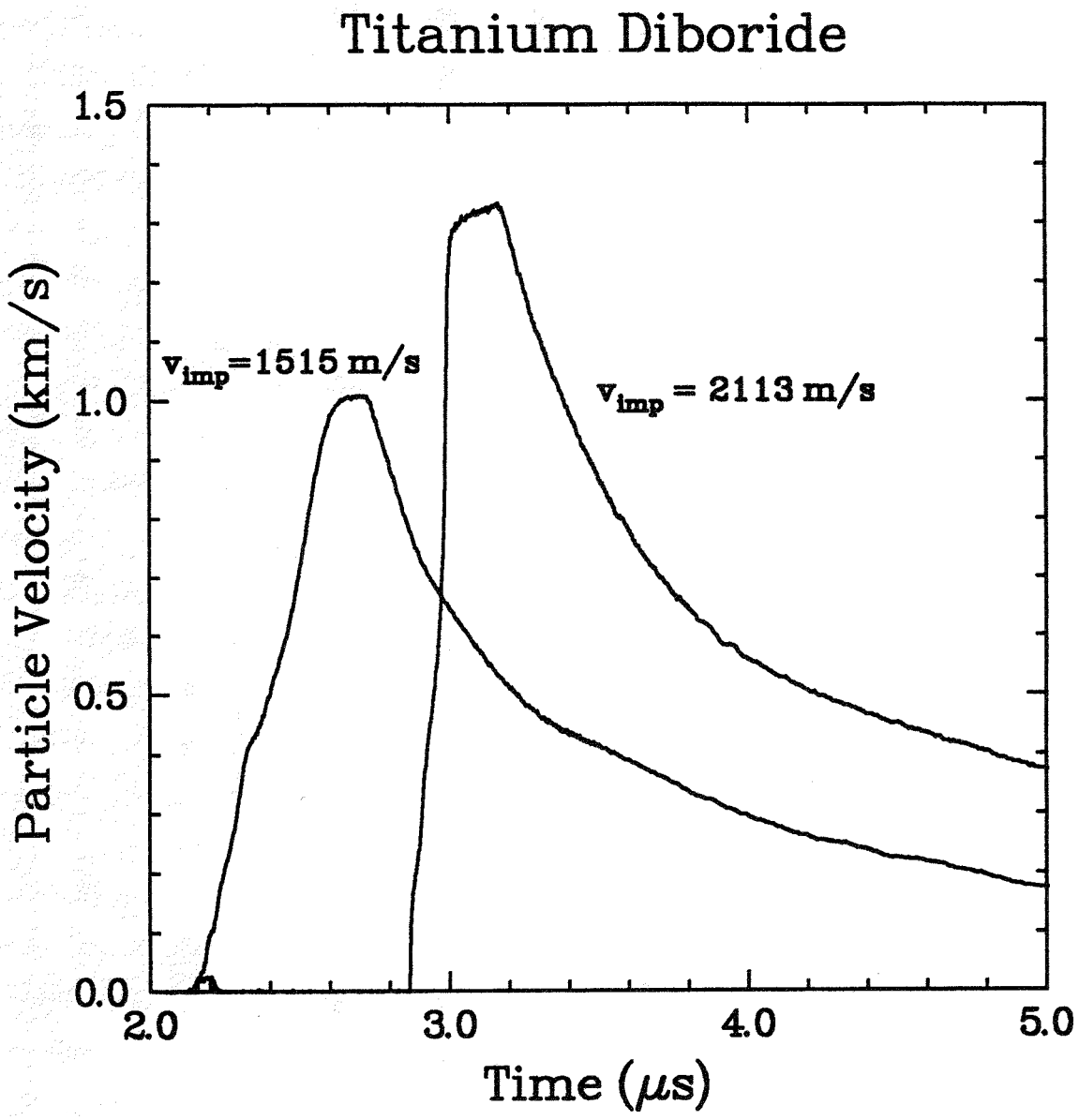

Figure 4: Titanium diboride particle velocity histories for 1.5 and 2.1 km/s symmetric plate impact velocities.

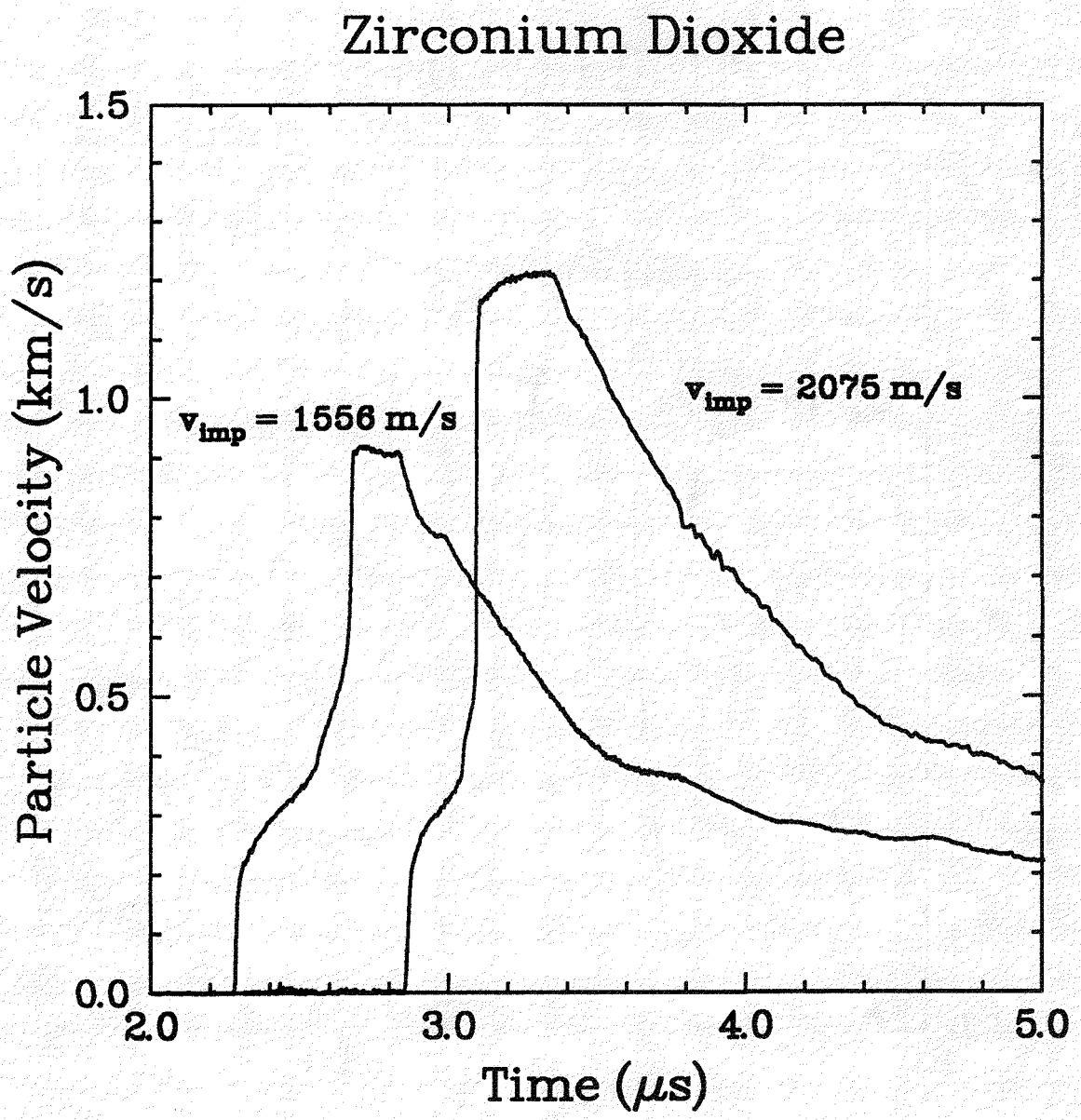

Figure 5: Zirconium dioxide particle velocity histories for 1.5 and 2.1 km/s symmetric plate impact velocities.

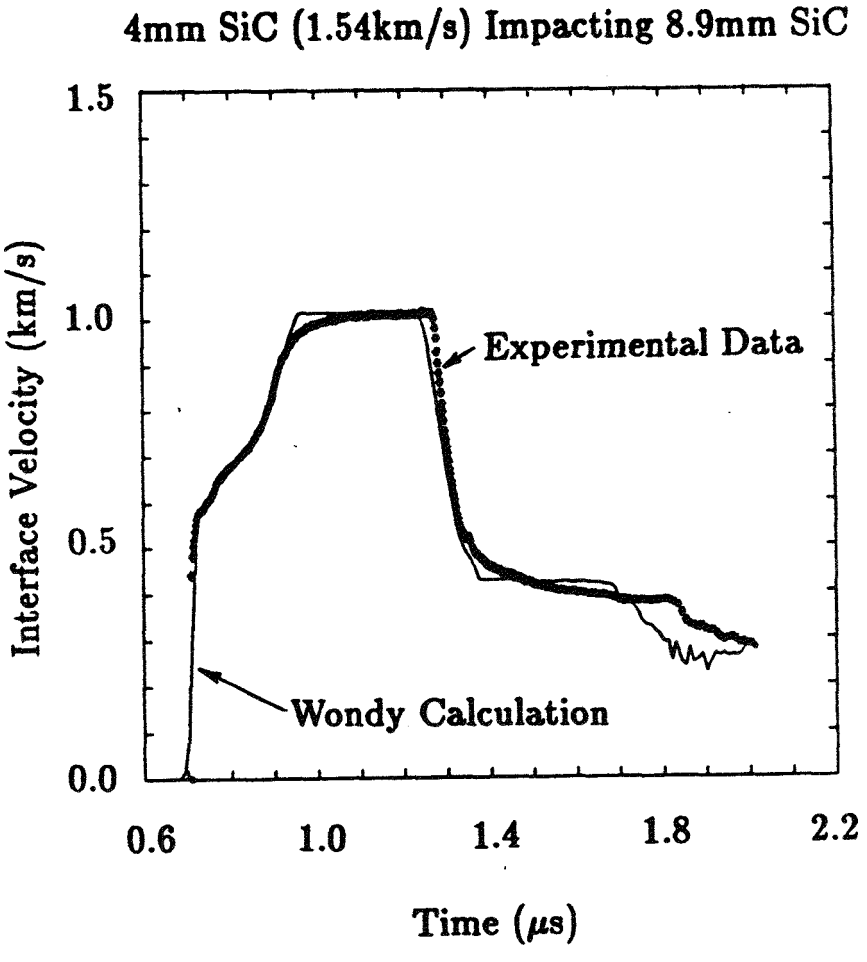

Figure 6: Silicon carbide particle velocity data and WONDY calculation (1.5 km/s).

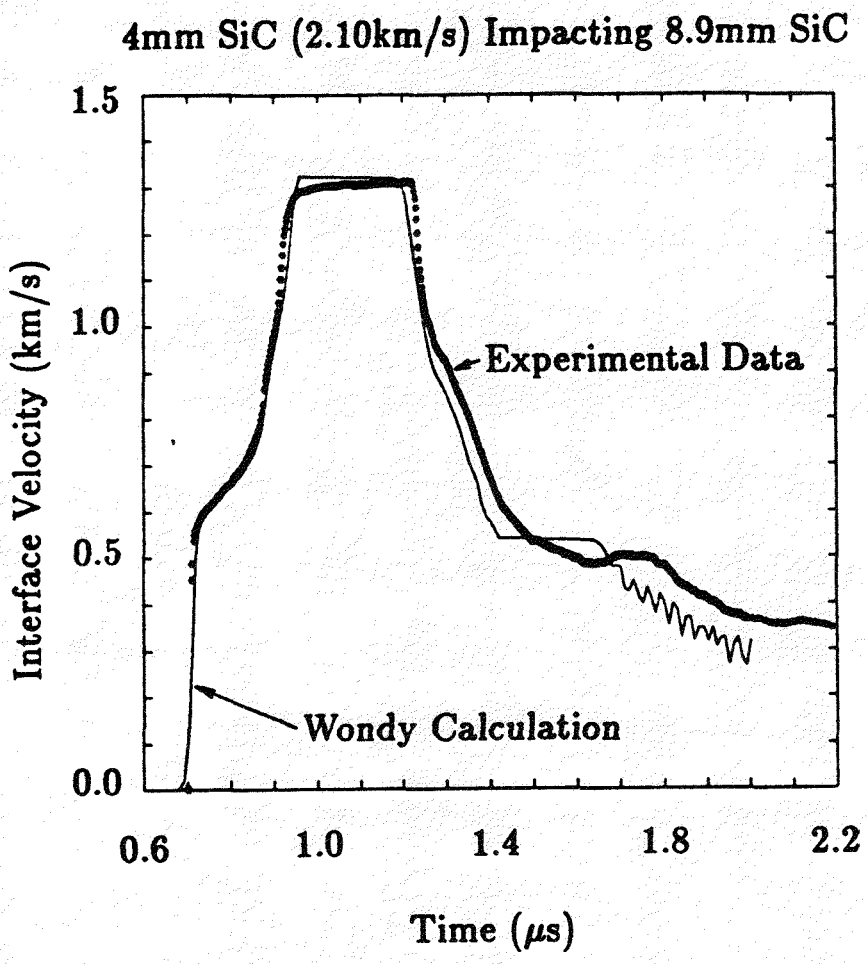

Figure 7: Silicon carbide particle velocity data and WONDY calculation (2.1 km/s).

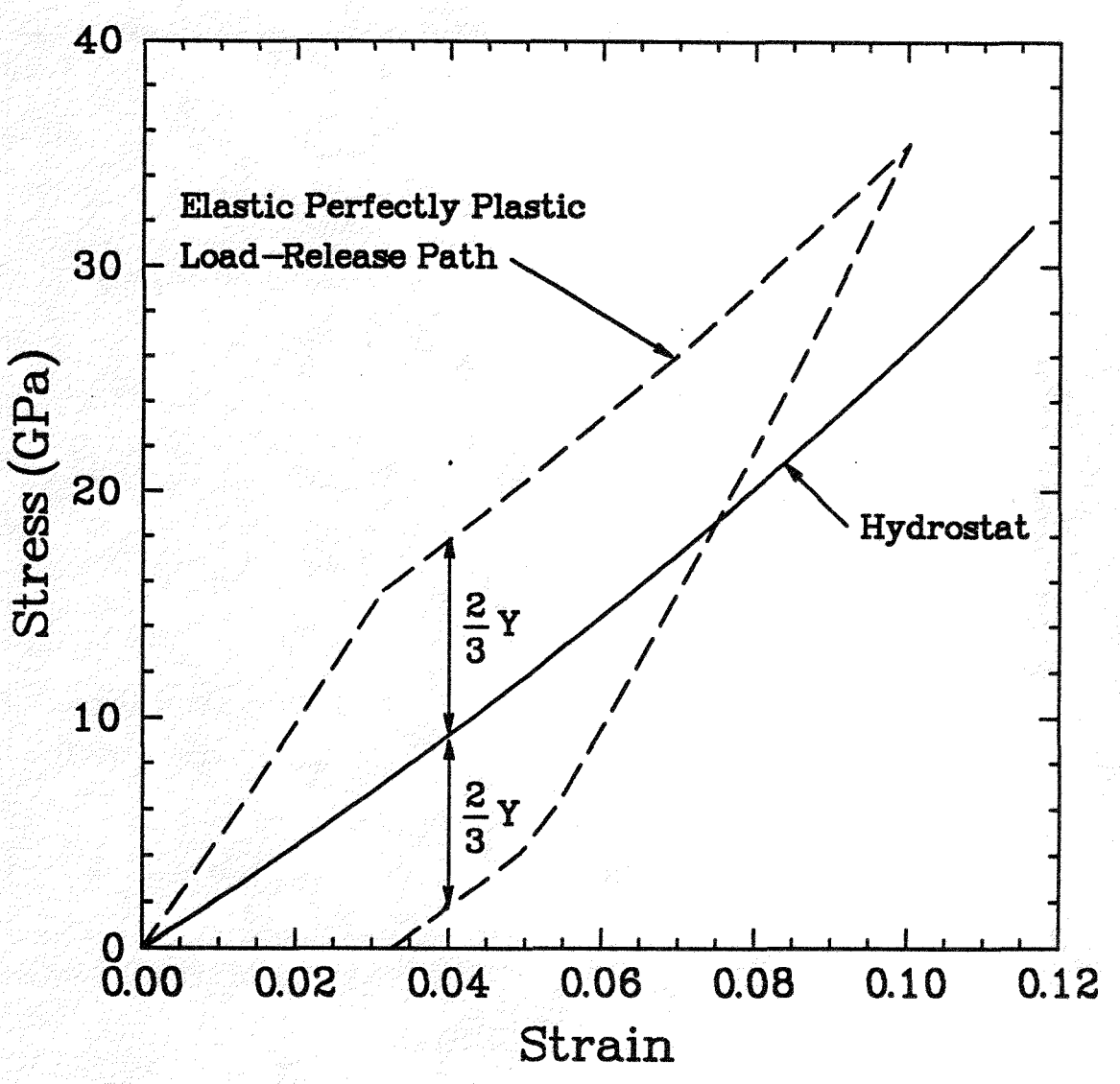

Figure 8: Calculated elastic-perfectly plastic stress-strain path in a silicon carbide target.

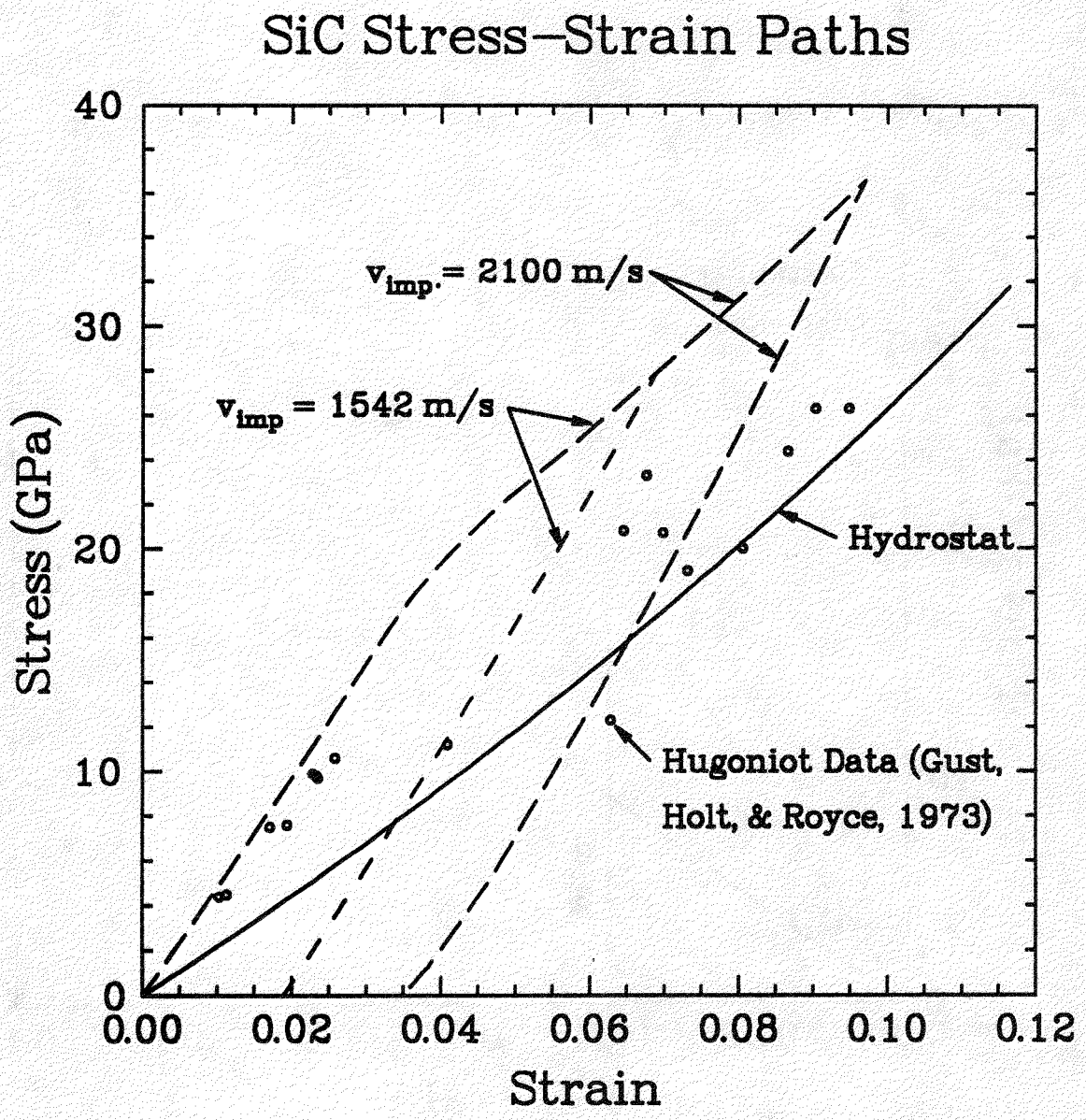

Figure 9: Calculated strain-hardening plasticity stress-strain paths in silicon carbide (1.5 and 2.1 km/s).

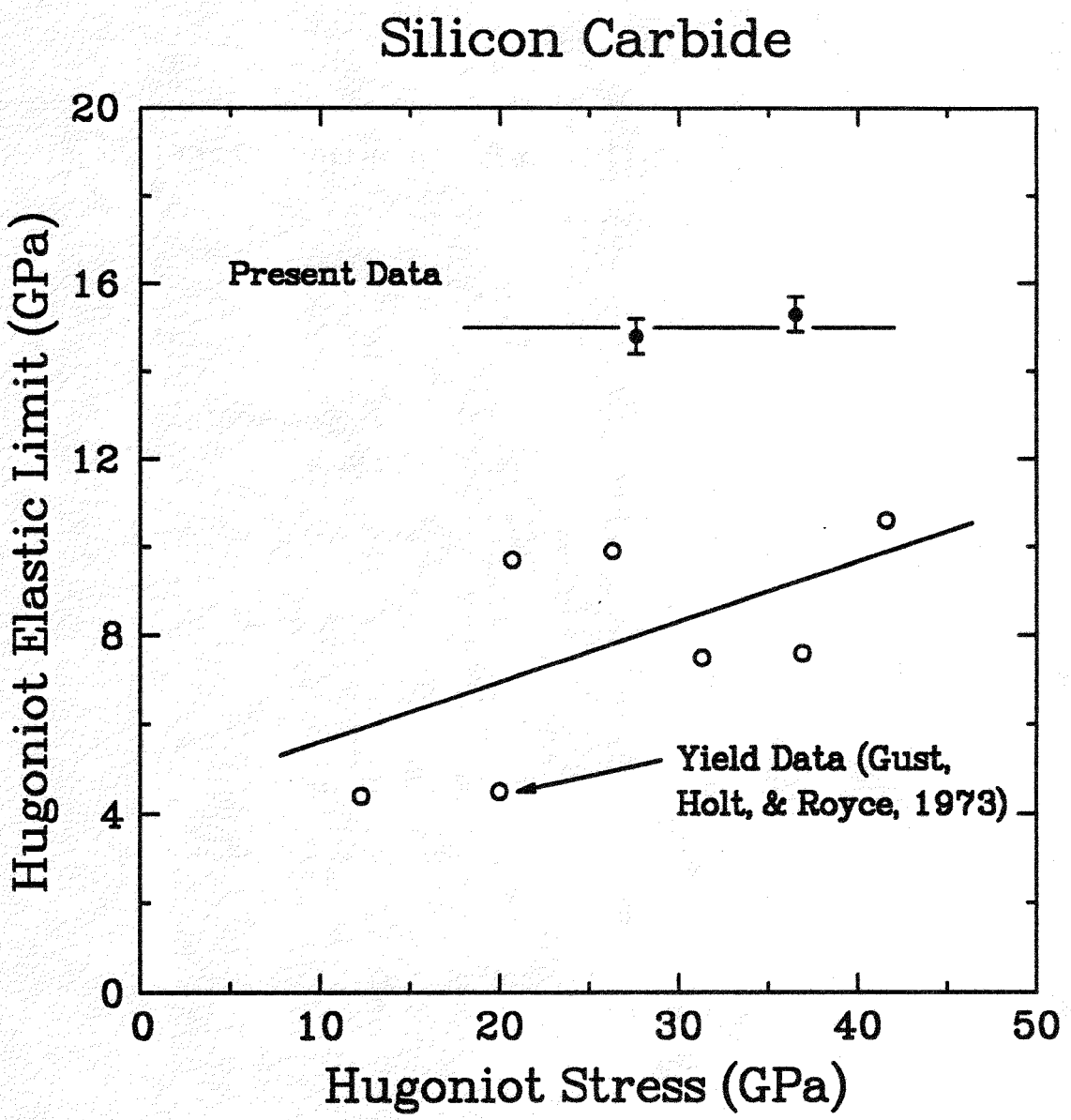

Figure 10: Hugoniot Elastic Limit data as a function of Hugoniot pressure state for silicon carbide.

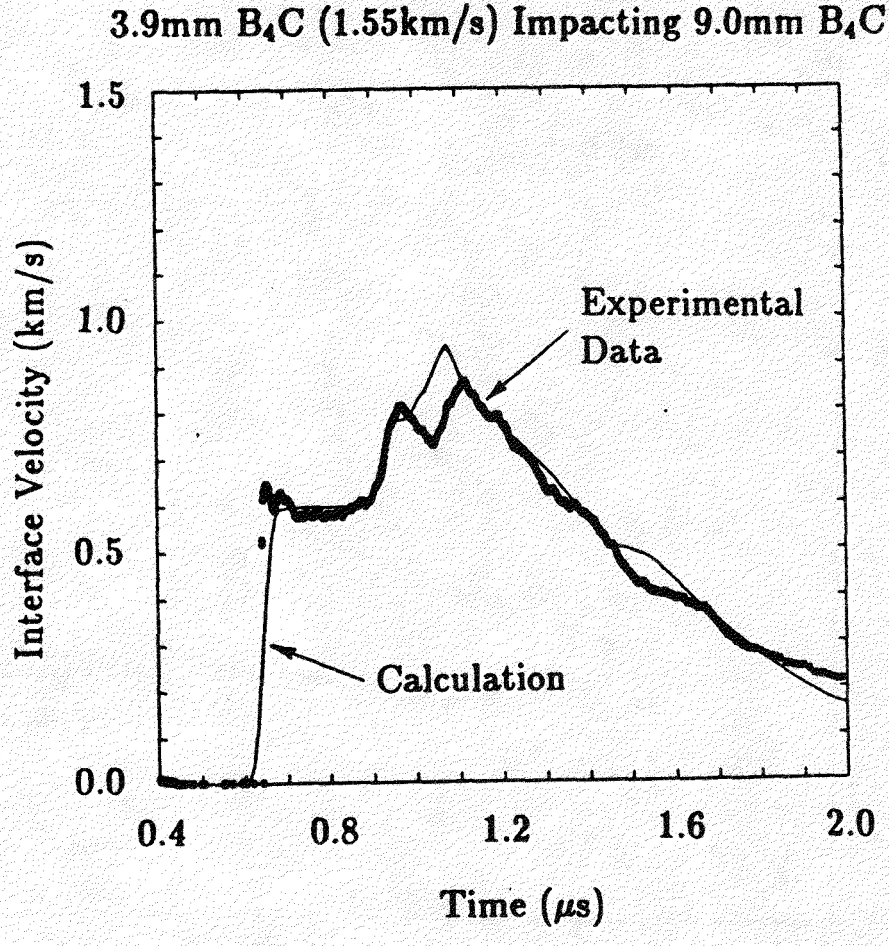

Figure 11: Boron carbide particle velocity data and WONDY calculation (1.5 km/s).

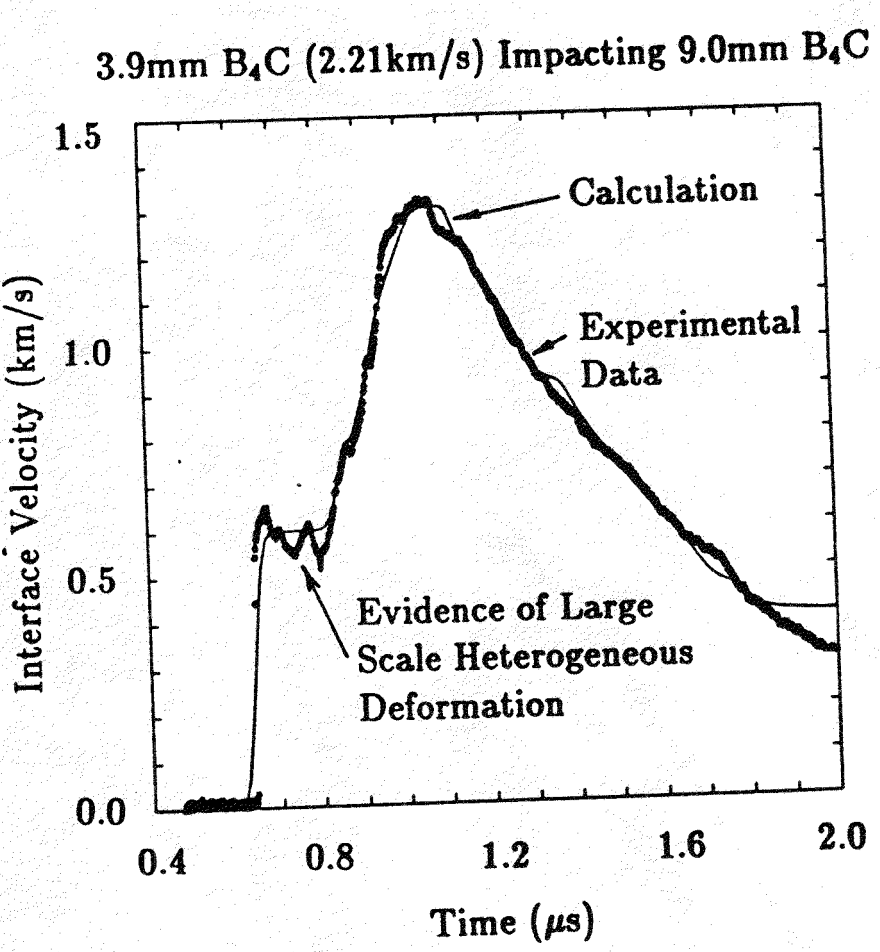

Figure 12: Boron carbide particle velocity data and WONDY calculation (2.2 km/s).

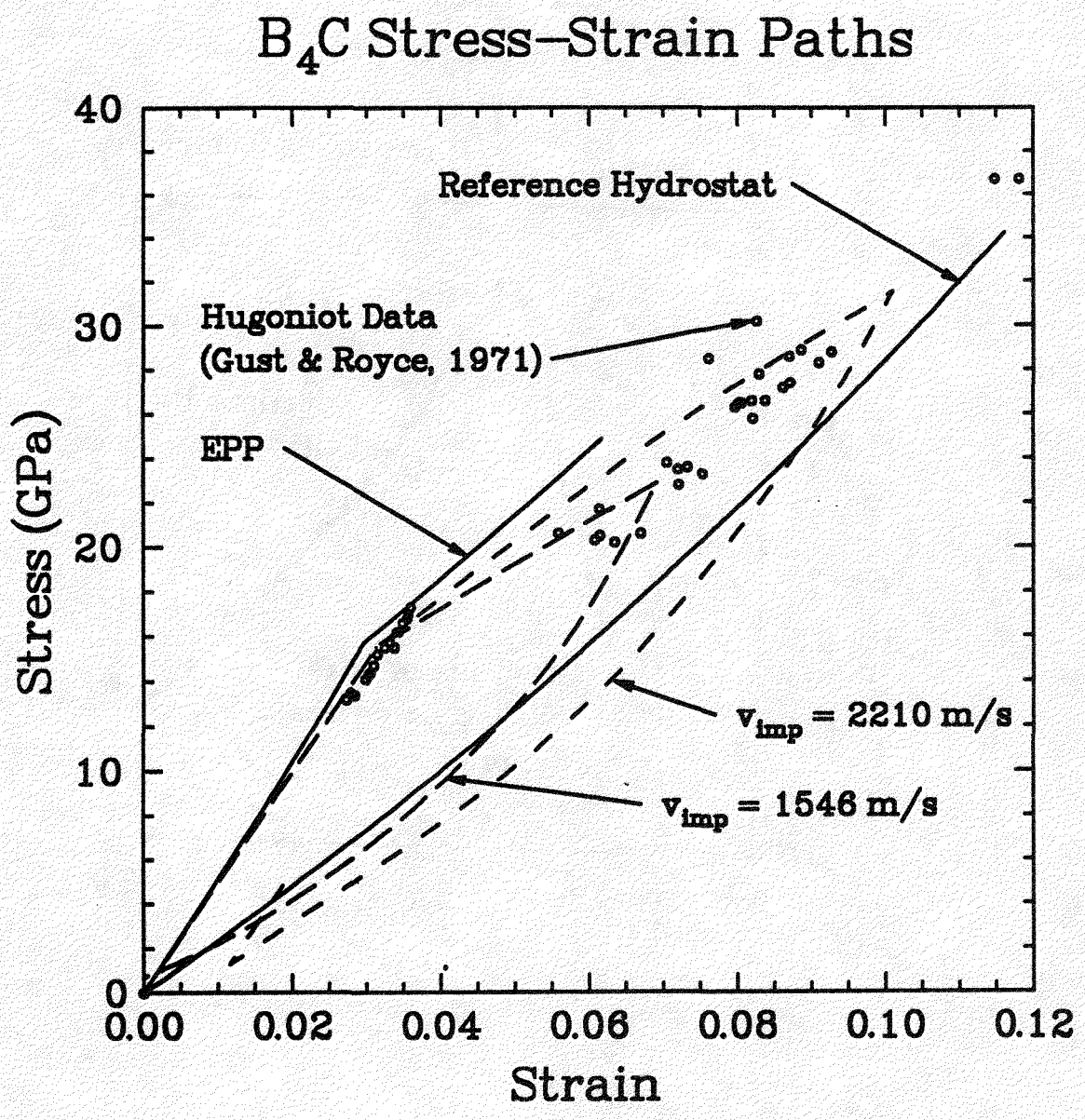

Figure 13: Calculated stress-strain paths in boron carbide (1.5 and 2.1 km/s).

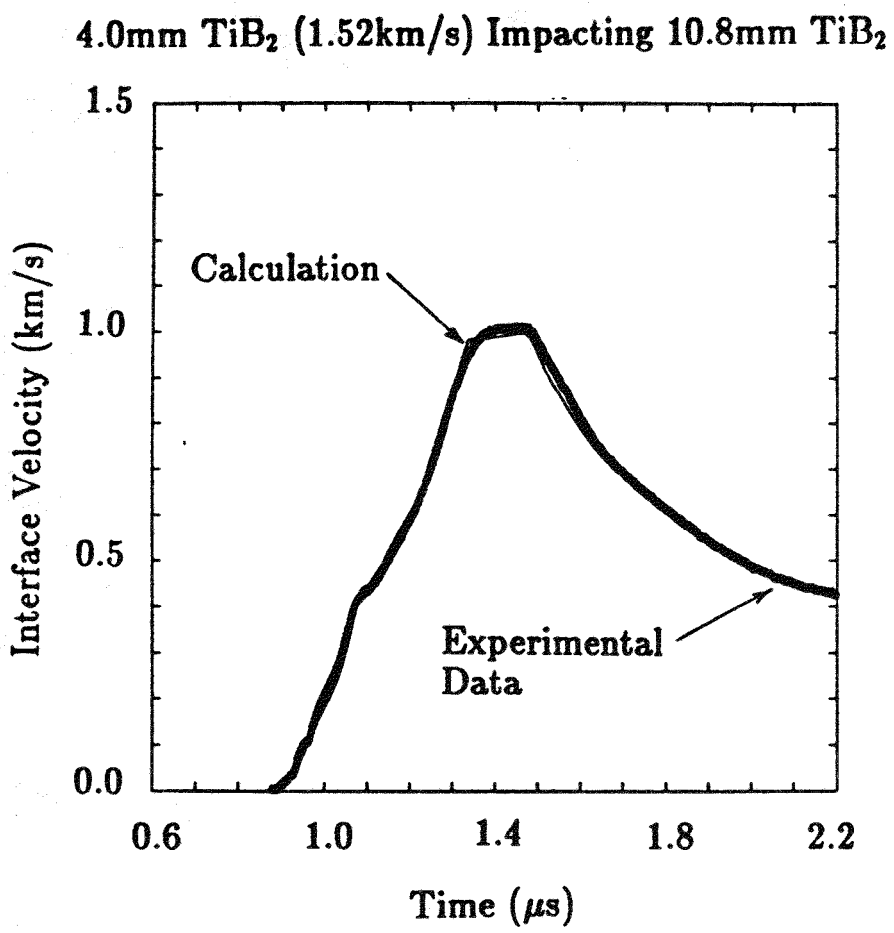

Figure 14: Titanium diboride particle velocity data and WONDY calculation (1.5 km/s).

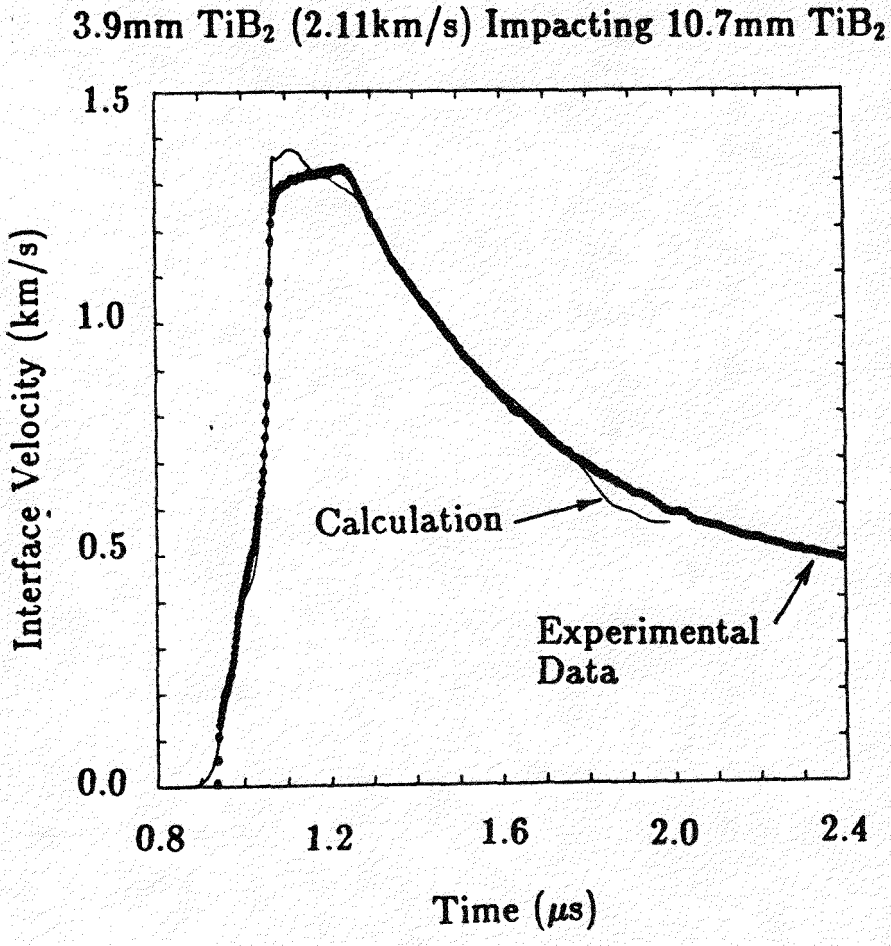

Figure 15: Titanium diboride particle velocity data and WONDY calculation (2.1 km/s).

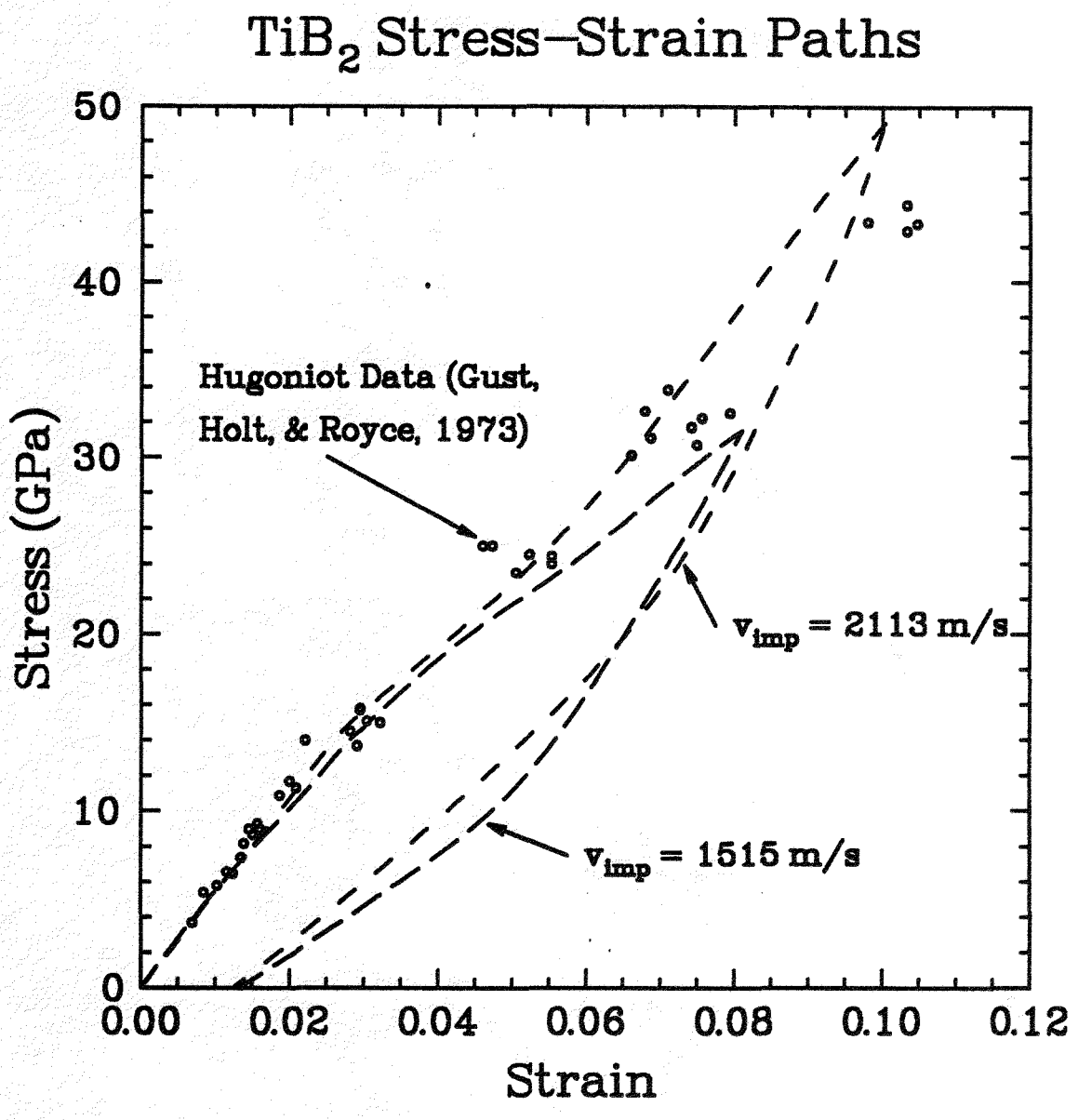

Figure 16: Calculated stress-strain paths in titanium diboride (1.5 and 2.1 km/s).

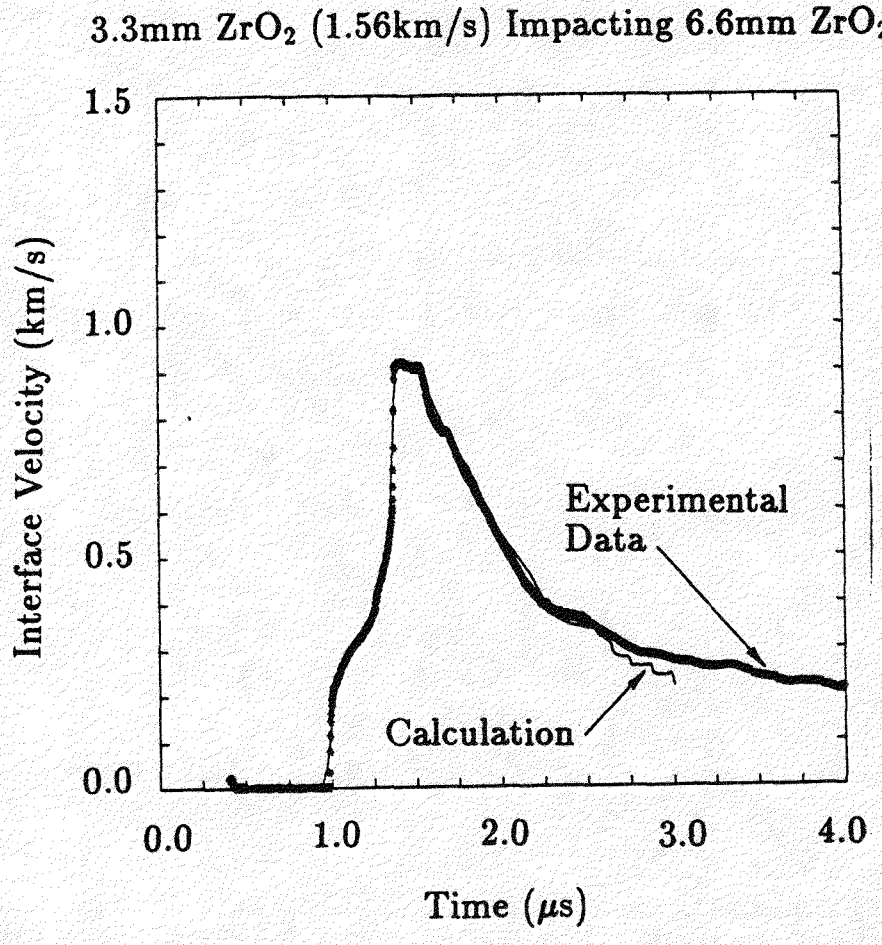

Figure 17: Zirconium dioxide particle velocity data and WONDY calculation (1.5 km/s).

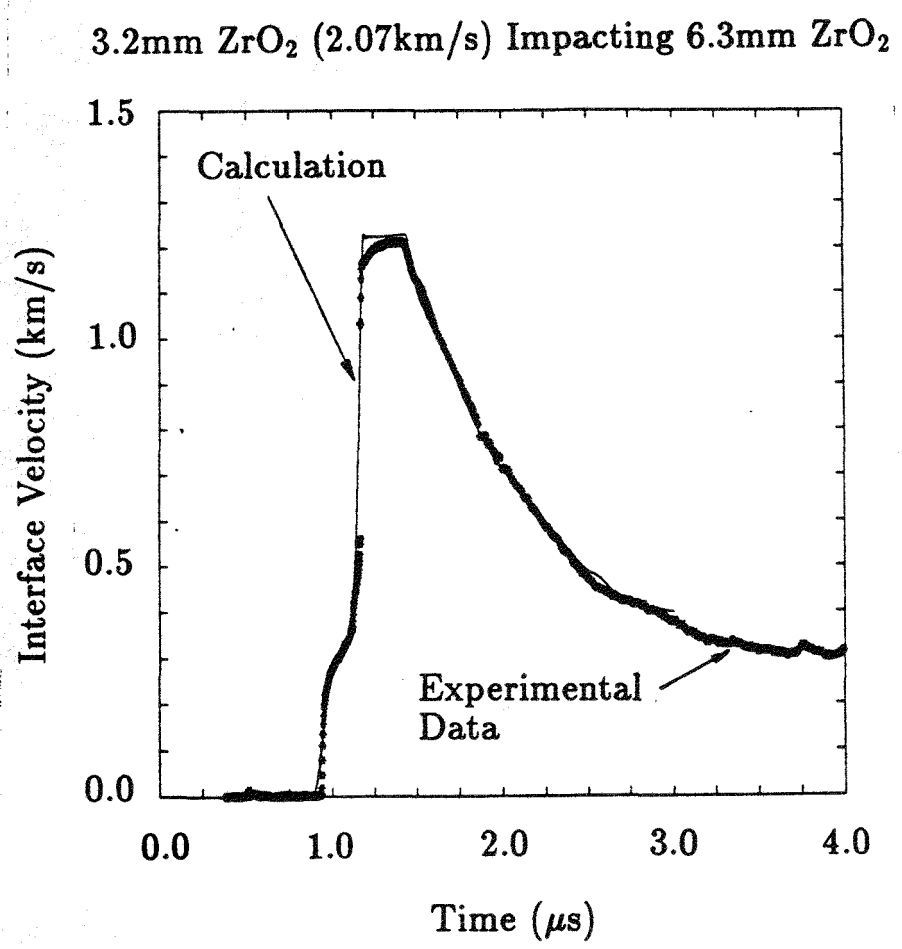

Figure 18: Zirconium dioxide particle velocity data and WONDY calculation (2.1 km/s).

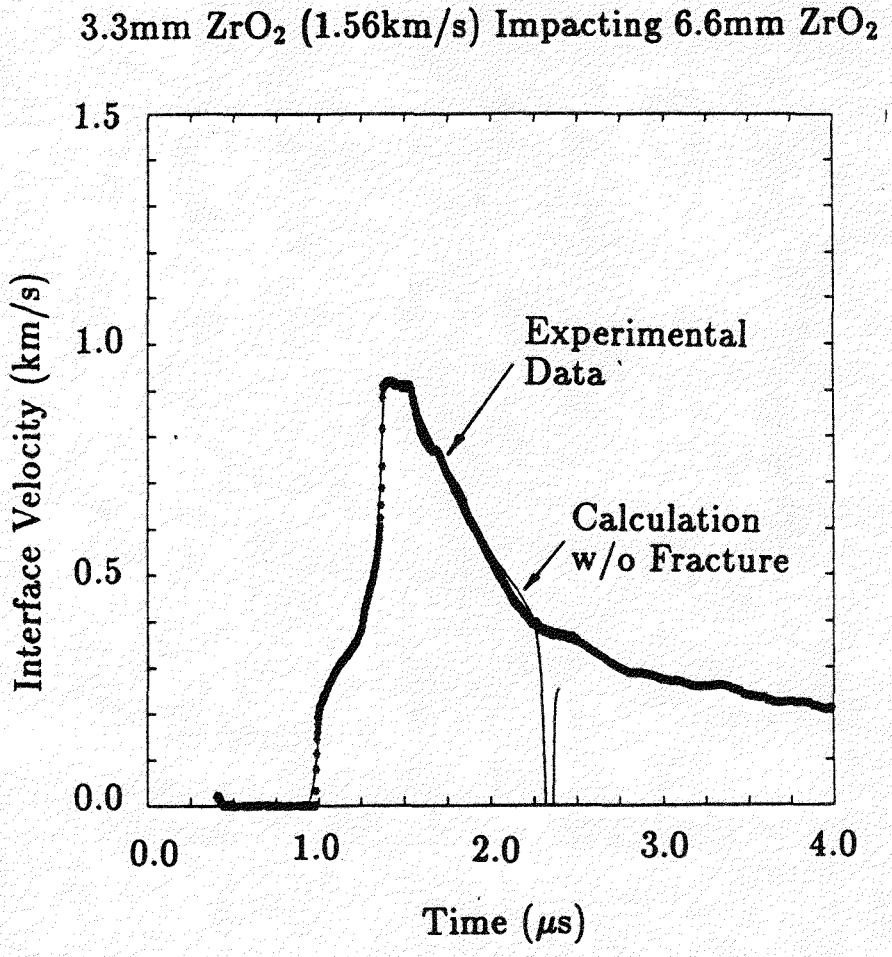

Figure 19: Zirconium dioxide particle velocity data and WONDY calculation with fracture suppressed (1.5 km/s).

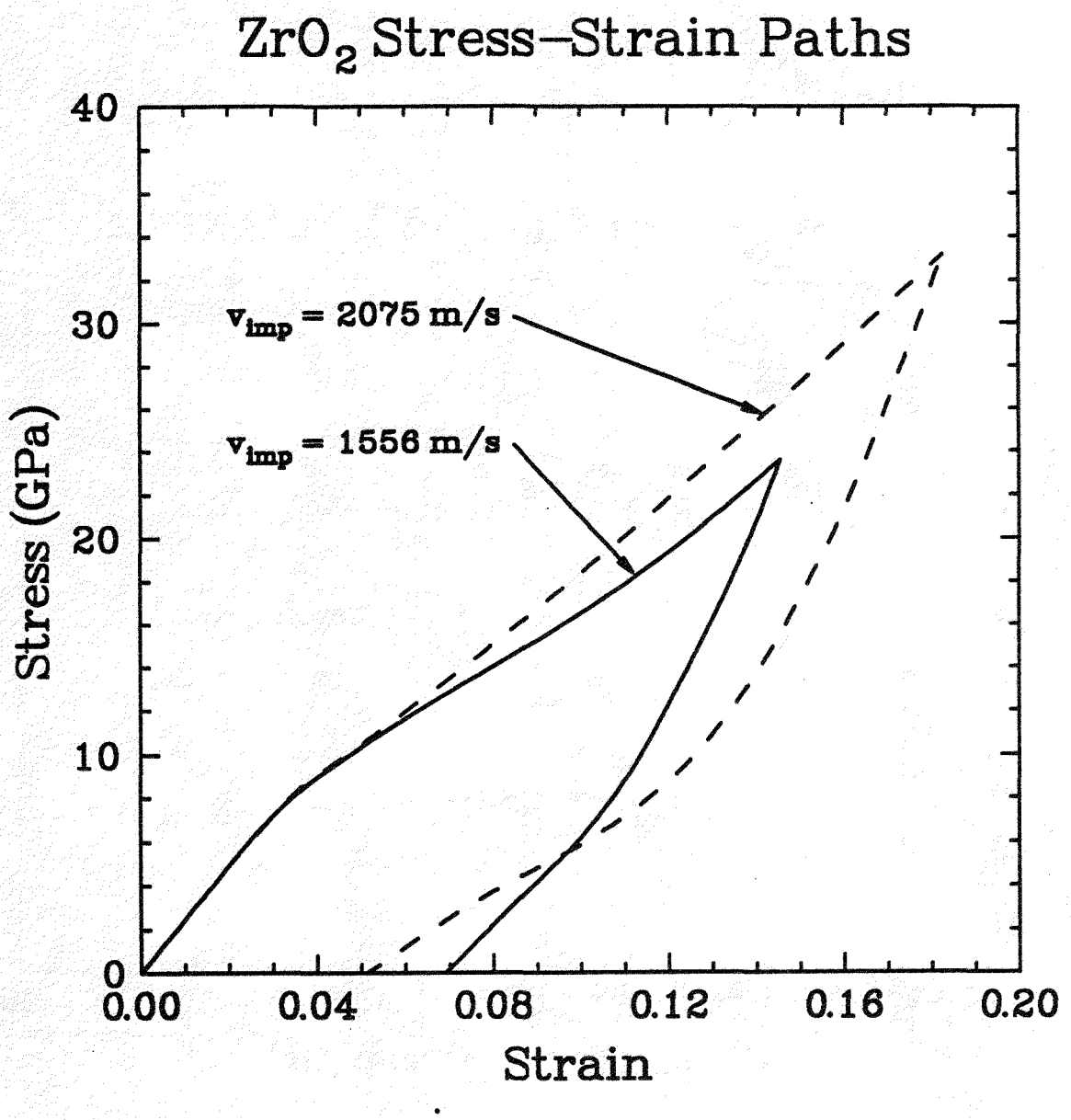

Figure 20: Calculated stress-strain paths in zirconium dioxide (1.5 and 2.1 km/s).

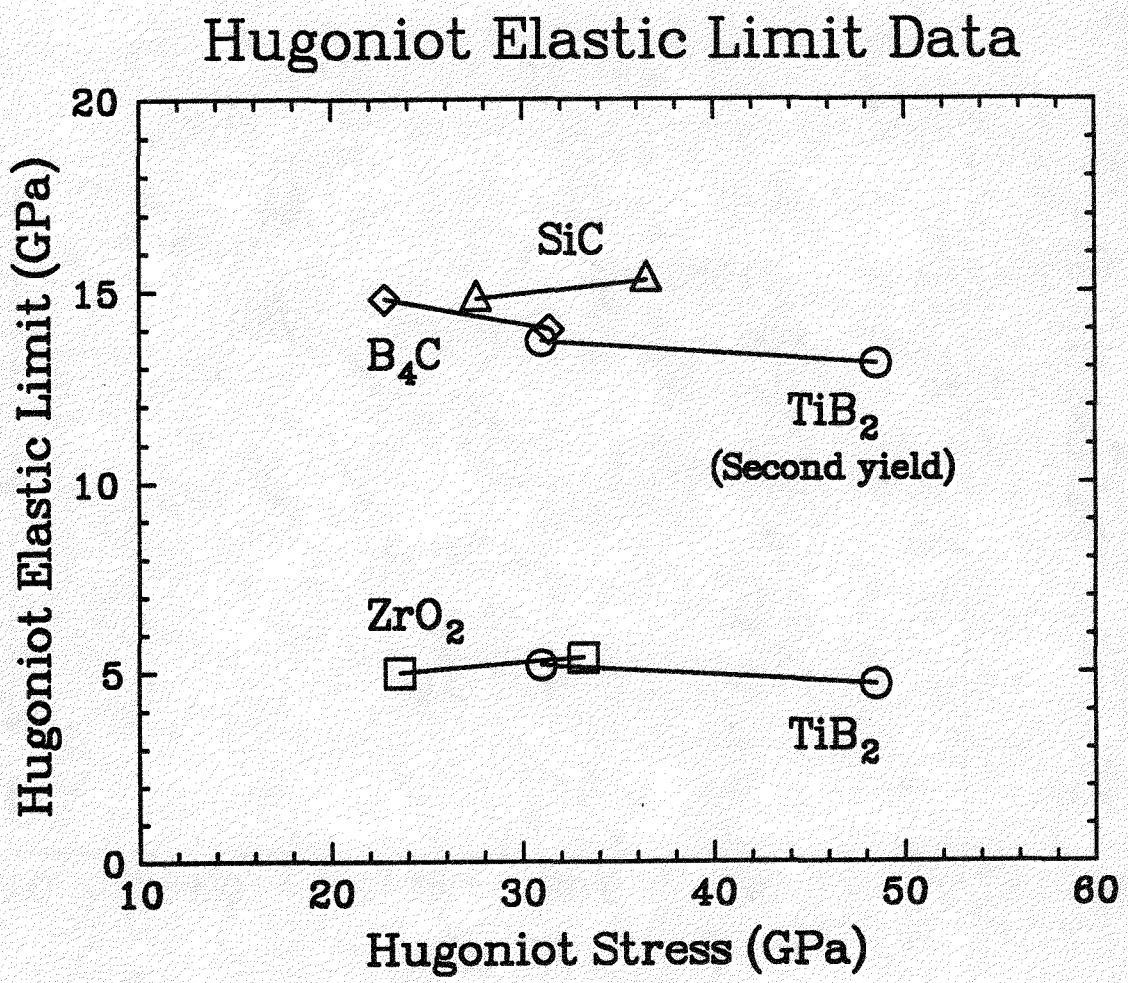

Figure 21: Summary of Hugoniot Elastic Limit data for the present experiments plotted against Hugoniot stress.

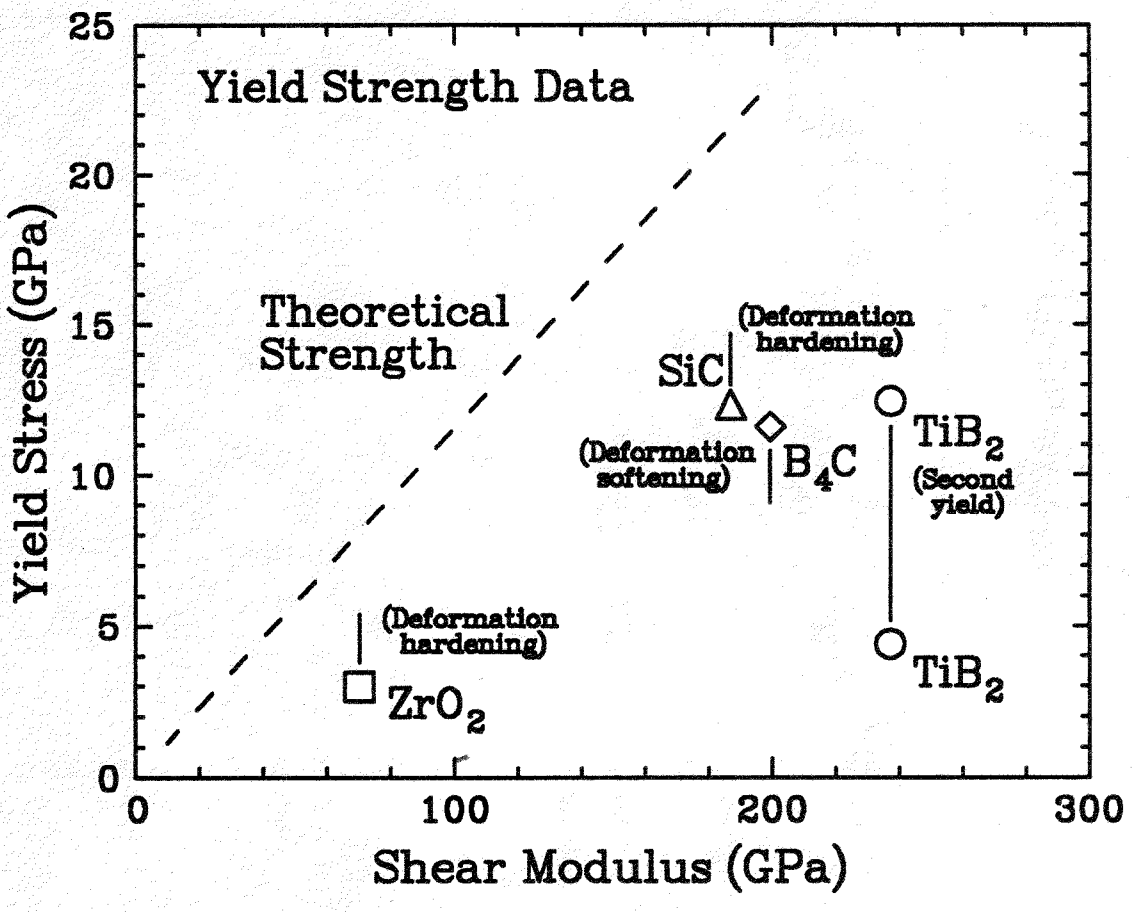

Figure 22: Summary of yield strength data for the present experiments plotted against shear modulus.

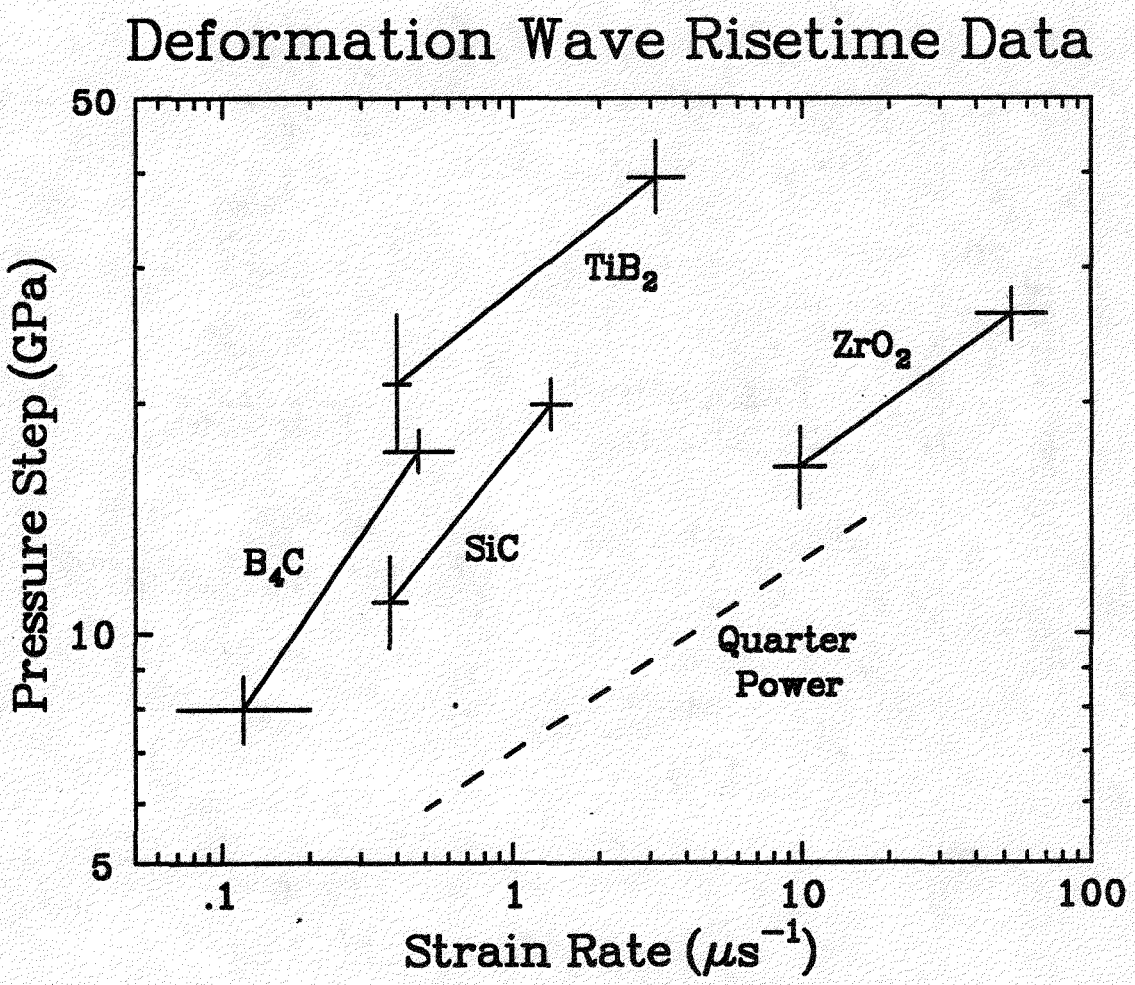

Figure 23: Summary of deformation wave amplitude data for the eight experiments reported plotted against risetime strain rate.

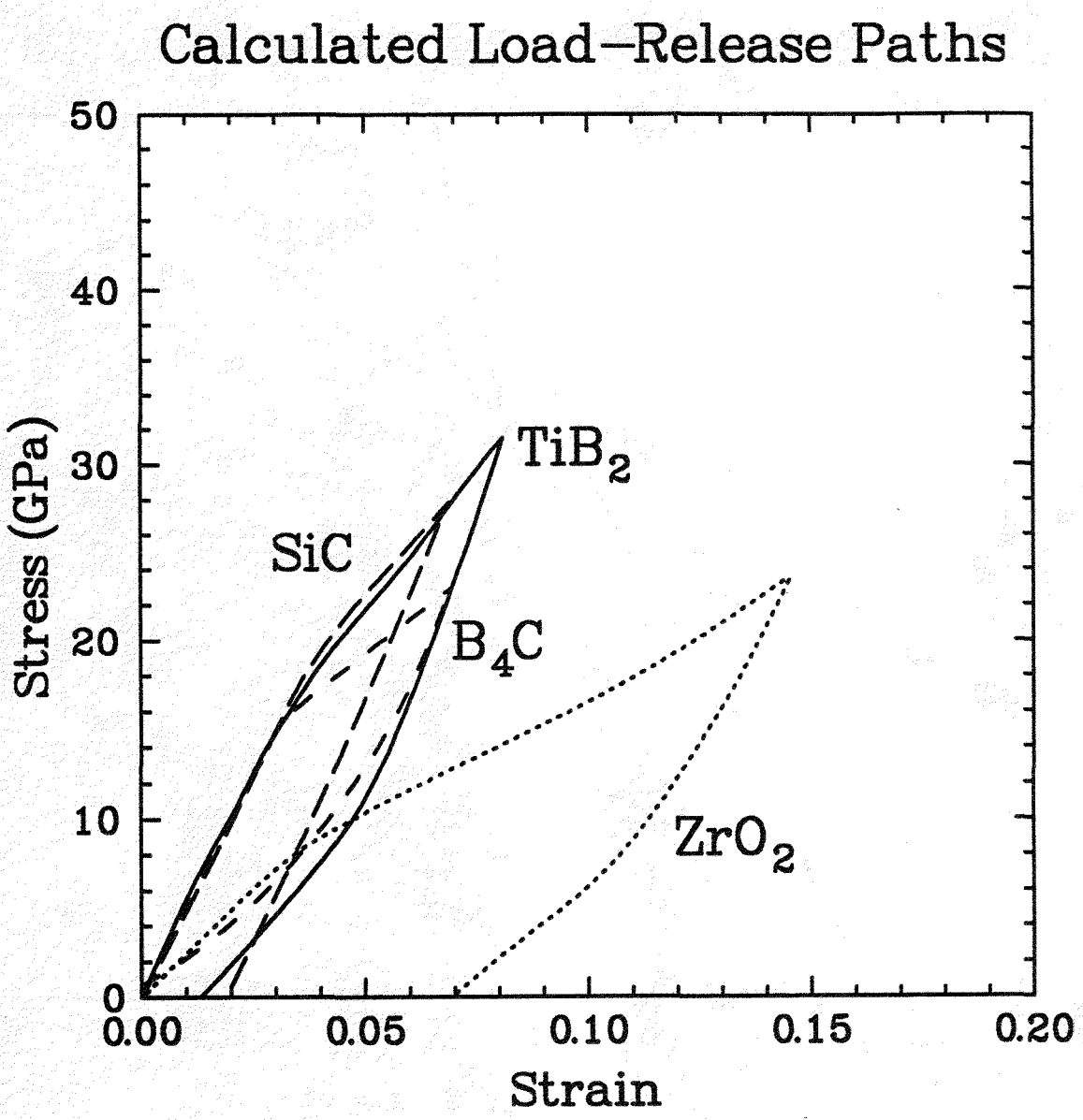

Figure 24: Summary of calculated load-release paths for the four low amplitude experiments.

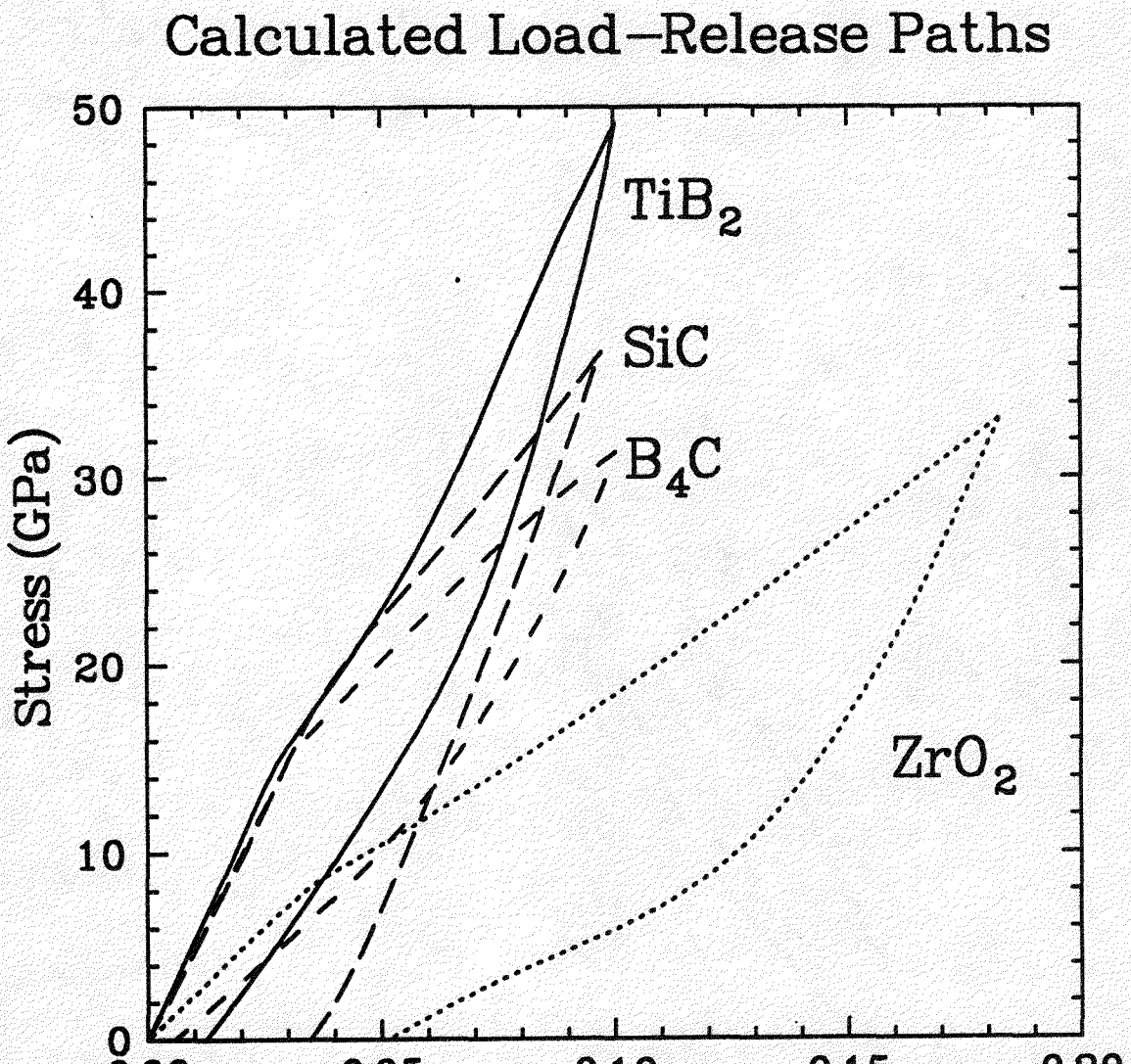

Figure 25: Summary of calculated load-release paths for the four high amplitude experiments.

DISTRIBUTION:

Dr. Marc A. Adams
JPL MS 97-B
4800 Oak Grove Dr.
Pasadena, CA 91109

Thomas F. Adams, X-3, MS F663
Los Alamos National Laboratory
Los Alamos, NM 87545

Dr. F. Adessio, T-3, MS B216
Los Alamos National Laboratory
Los Alamos, NM 87545

I. Ahmed
U.S.Army Research Office
P.O. Box 12211
Research Triangle Park, NC 27709

Professor T. J. Ahrens
Geophysics Division MS/252-21
California Institute of Technology
Pasadena, CA 91125

M. L. Alme
R & D Associates
301 A South West St
Alexandria, VA 22314

Dr. C. E. Anderson
Southwest Research Institute
6220 Culebra Road
San Antonio, TX 78284

Dr. S. J. Bless
Univ of Dayton Research Inst
300 College Park, KLA-14
Dayton, OH 45469-0001

Dr. W. R. Blumenthal, MST-5, MS E546
Los Alamos National Laboratory
Los Alamos, NM 87545

M. W. Burkett, WX-4, MS G787
Los Alamos National Laboratory
Los Alamos, NM 87545

P. D. Buckley
NMIMT, TERA Group
Socorro, NM 87801

J. Carleone
Aerojet Ordnance Company
2521 Michelle Drive
Tustin, CA 92680

E. J. Chapyak, X-3, MS F663
Los Alamos National Laboratory
Los Alamos, NM 87545

Dr. S. C. Chou
US Army Materials Tech Lab
SLCMT-MRD
Arsenal Street
Watertown, MA 02172-0001

W. H. Cook
Air Force Armament Laboratory
Eglin Air Force Base, Florida 32542-5434

G. E. Cort, ATAC, MS K574
Los Alamos National Laboratory
Los Alamos, NM 87545

Andrew Crowson
Army Research Office
P.O. Box 12211
Research Triangle Park, NC 27709

D. Curran
SRI International
333 Ravenswood Ave
Menlo Park, CA 94025

Dr. D. P. Dandekar
US Army Materials Tech Lab
Arsenal Street
Watertown, MA 02172

Dr. M. Finger, L-38
Lawrence Livermore National Laboratory
Livermore, CA 94550

Dr. P. S. Follansbee, MST-5, MS G730
Los Alamos National Laboratory
Los Alamos, NM 87545

J. C. Foster, Jr.
Air Force Armament Laboratory
Eglin Air Force Base, Florida 32542-5434

J. Furlong
R & D Associates
301 A South West St
Alexandria, VA 22314

Dr. L. A. Glenn, MS-L200
Lawrence Livermore National Laboratory
Livermore, CA 94550

G. E. Hauver
US Army Ballistic Research Lab
AMB-TBD
Aberdeen Proving Ground, MD 21005-5066

G. A. Hegemier
Trans Science Corporation
P.O. Box 2727
La Jolla, CA 92038

T. Holmquist
Honeywell, Incorporated
7225 Northland Drive
Brooklyn Park, MN 55428

Wm. H. Holt
Nval Code G35
Naval Surface Warfare Center
Dahlgren, VA 22448

G. R. Johnson
Honeywell, Incorporated
7225 Northland Drive
Brooklyn Park, MN 55428

Dr. J. N. Johnson, T-14, MSB214
Los Alamos National Laboratory
Los Alamos, NM 87545

R. Karpp, M-8, MS J960
Los Alamos National Laboratory
Los Alamos, NM 87545

K. Kimsey
US Army Ballistic Research Lab
AMB-TBD
Aberdeen Proving Ground, MD 21005-5066

R. L. Landingham, MC L-369
Lawrence Livermore National Laboratory
Livermore, CA 94550

James Lankford
Southwest Research Institute
6220 Culebra Road
San Antonio, TX 78284

Dr. P. J. Mauldlin, N-6, MS K557
Los Alamos National Laboratory
Los Alamos, NM 87545

Dr. George Mayer
Institute for Defense Analysis
1801 N. Beauregard Street
Alexandria, VA 22311-1772

T. L. Menna
General Research Corporation
5383 Hollister Ave
Santa Barbara, CA 93160-6770

J. Mescall
US Army Materials Tech Lab
SLCMT-MRD
Arsenal Street
Watertown, MA 02172-0001

J. Morrow, MD 320
FMC Corporation
881 Martin Ave
Santa Clara, CA 95052

G. L. Moss
Lanxide Corporation
1 Tralee Industrial Park
Newark, DE 19714-6077

S. Nemat-Nasser
University of California, San Diego
Department of AMES, R-011
La Jolla, CA 92093

D. L. Orphal
California Research & Technology Inc
5117 Johnson Dr
Pleasanton, CA 94566

Dr. F. W. Patten
DARPA/Materials Science Office
1400 Wilson Blvd.
Arlington, VA 22209-2308

A. Rajendran
Univ of Dayton Research Inst
300 College Park, KLA-14
Dayton, OH 45469-0001

G. Randers-Pehrson
U.S. Army Ballistics Research Laboratory
SLCBR-TB-AM
Aberdeen, MD 21005-5006

J. E. Reaugh, L-290
Lawrence Livermore National Laboratory
Livermore, CA 94550

J. Repa, DRA-CDT, MS F668
Los Alamos National Laboratory
Los Alamos, NM 87545

S. Segletes
US Army Ballistic Research Lab
SLCBR-TB-P
Aberdeen Proving Ground, MD 21005-5066

Dr. D. R. Shockey
SRI International
333 Ravenswood Ave
Menlo Park, CA 94025

W. E. Snowden
ODDR&E
The Pentagon
Washington, DC 20305

J. W. Straight, M-8, MS J960
Los Alamos National Laboratory
Los Alamos, NM 87545

LTC P. H. Sullivan
DARPA/TTO - A/A(2)
1400 Wilson Blvd
Arlington, VA 22209-2308

J. Taylor, ADDRA, MS A110
Los Alamos National Laboratory
Los Alamos, NM 87545

D. J. Viechniki
US Army Materials Tech Lab
SLCMT-MCC
Arsenal Street
Watertown, MA 02172-0001

B. Wilcox
DARPA/Materials Science Office
1400 Wilson Blvd.
Arlington, VA 22209-2308

M. L. Wilkins
Lawrence Livermore National Laboratory
Livermore, CA 94550

P. Woolsey
US Army Materials Tech Lab
SLCMT-MRD
Arsenal Street
Watertown, MA 02172-0001

Thomas W. Wright
U.S. Army Ballistics Research Laboratory
SLCBR-TB-W
Aberdeen Proving Ground, MD 21005

F. J. Zerilli
Code R13
Naval Surface Warfare Center
Silver Spring, MD 20903-5000

Sandia Internal:

1131 M. B. Boslough
1131 R. A. Graham
1510 J. W. Nunziato
1520 L. W. Davison
1530 D. B. Hayes
1531 S. L. Thompson
1531 J. M. McGlaun
1531 J. W. Swegle
1533 P. Yarrington
1533 P. J. Chen
1533 G. I. Kerley
1533 M. E. Kipp (25)
1533 S. T. Montgomery
1533 A. C. Robinson
1534 J. R. Asay
1534 L. M. Barker
1534 L. C. Chhabildas
1534 J. E. Dunn
1534 M. D. Furnish
1534 D. E. Grady (25)
1534 T. G. Trucano
1534 J. L. Wise
1550 C. W. Peterson
3141 S. A. Landenberger (5)
3141-1 C. A. Ward (8)
For DOE/TIC
3151 W. L. Garner (3)
6258 B. J. Thorne
8243 D. J. Bammann
9122 M. J. Forrestal
9122 V. K. Luk